地球惑星観測･探査学／惑星探査学２
「惑星大気の光学リモートセンシング」
Optical remote sensing of planetary atmospheres

新領域創成科学研究科　複雑理工学専攻
今村　剛

Observation methods

Merits and demerits

	Lander	Orbiter	Ground-based observation
Spatial coverage	Limited	Global	Global
Time coverage	Short in many cases	Long & continuous	Repeatable
Observable variables	- In-situ measurements - Many options	- Optical/radio remote sensing - In-situ plasma measurements - Small instruments	- Optical/radio remote sensing - Instruments can be large

Recent/future remote sensing (orbiter) missions

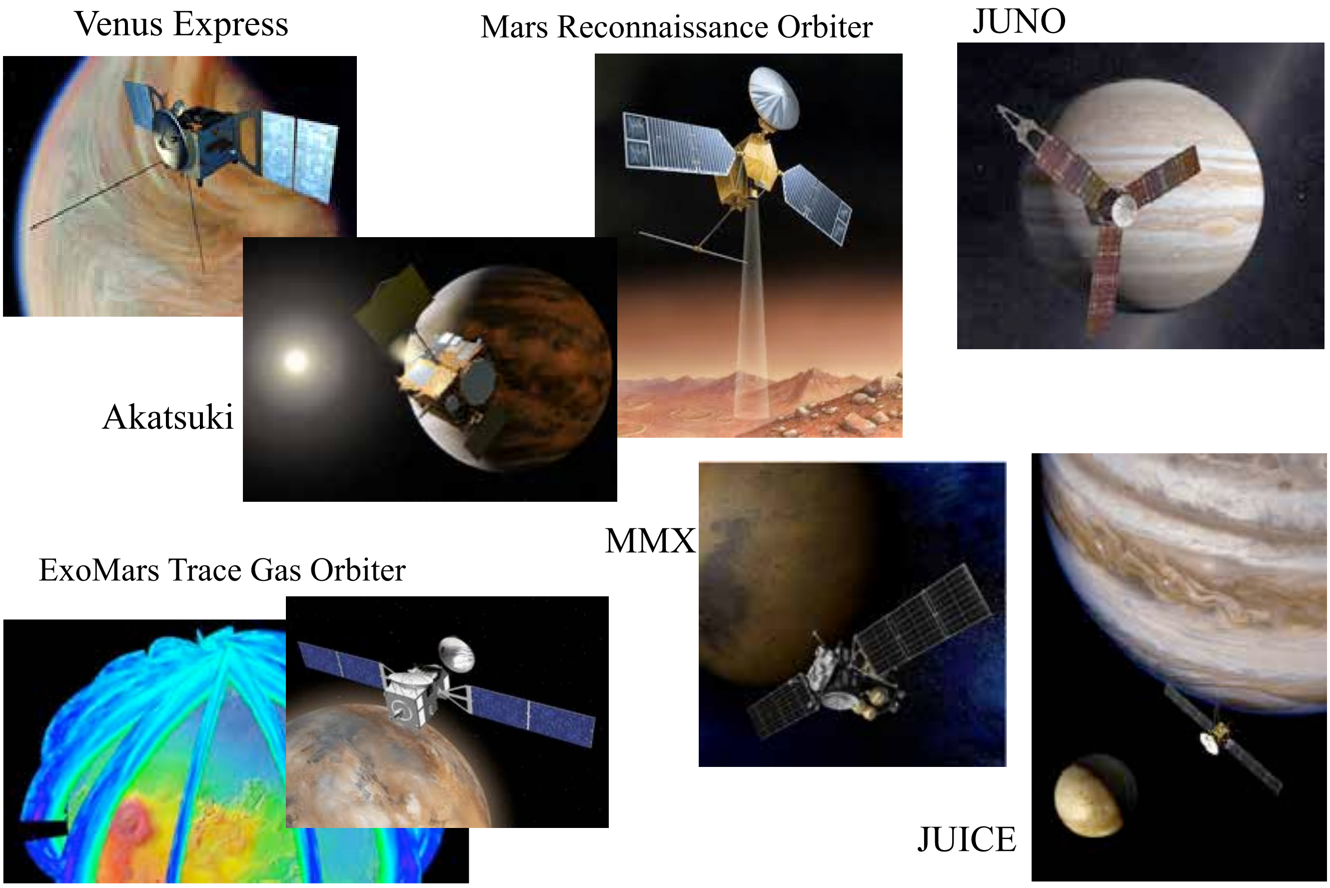

Interaction between molecules and electromagnetic waves

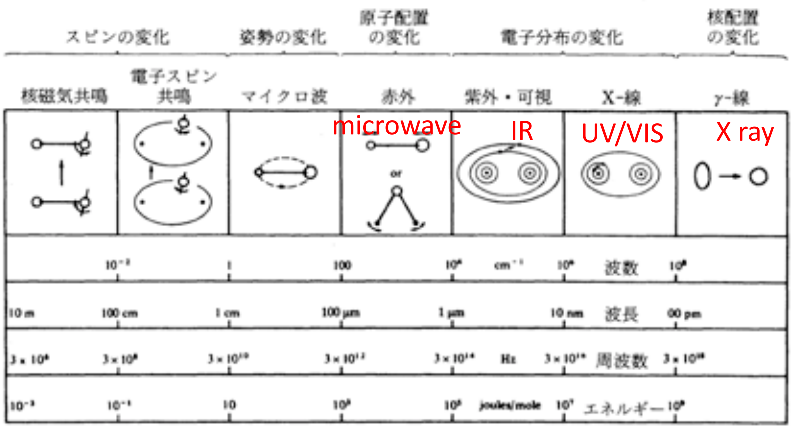

図 5.1 電磁波のスペクトルと電磁波–分子 (原子) の相互作用のメカニズム (Banwell and McCash, 1994)[26)]

柴田（1999）

Andrews (2010)

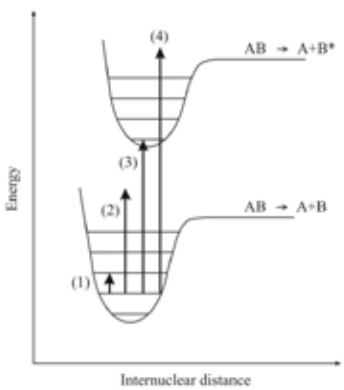

Schematic energy diagram for a diatomic molecule. See text for details.

Remote sensing of atmospheres

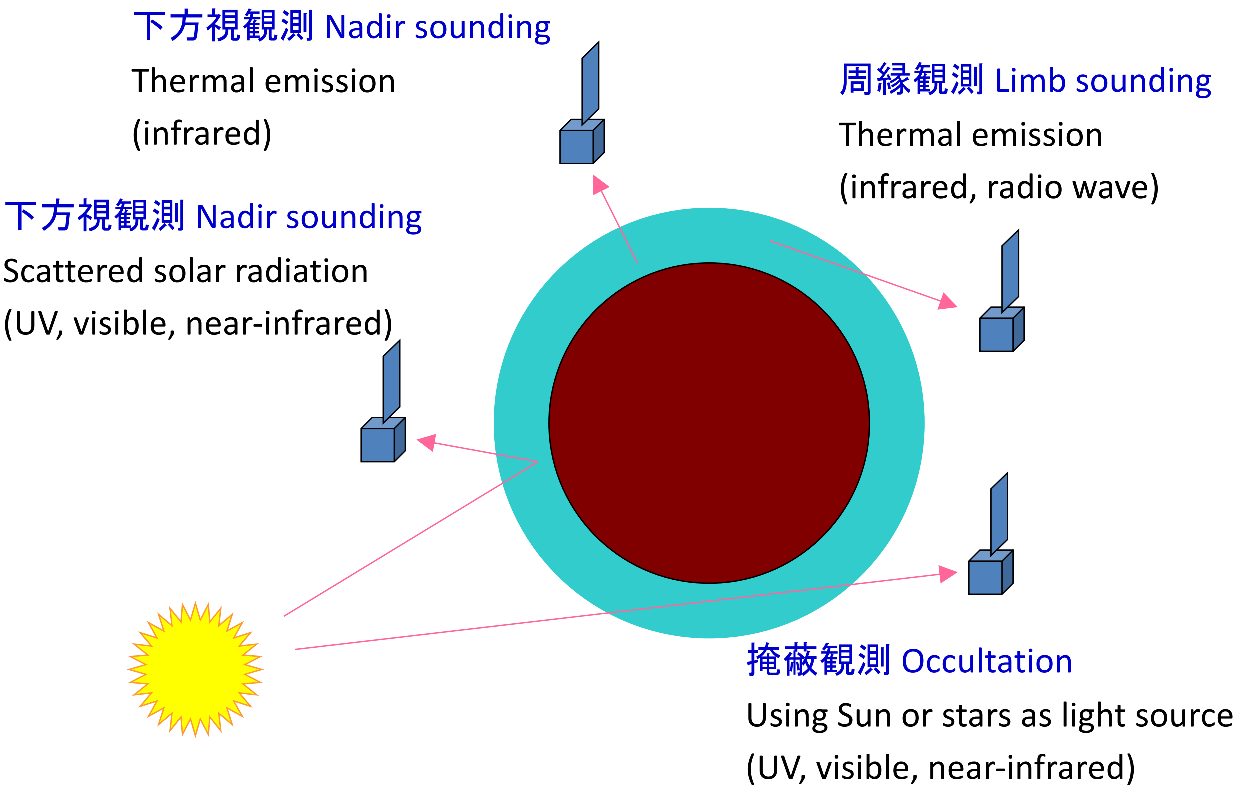

Imaging

Himawari (meteorological satellite) imaging channels

JMA Himawari HP

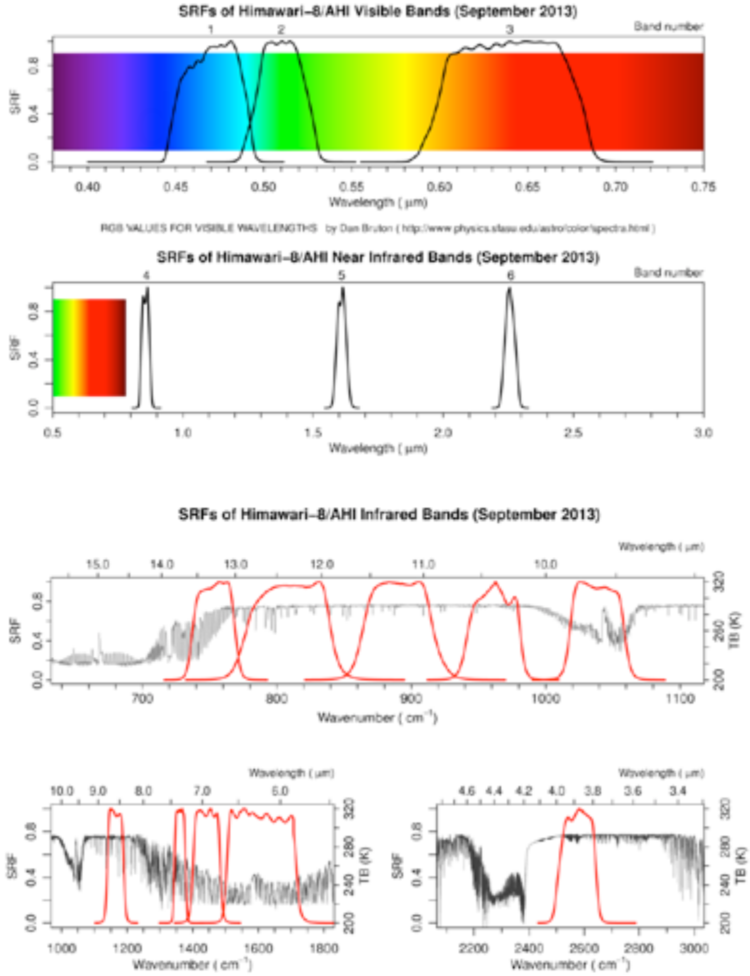

Interference filter

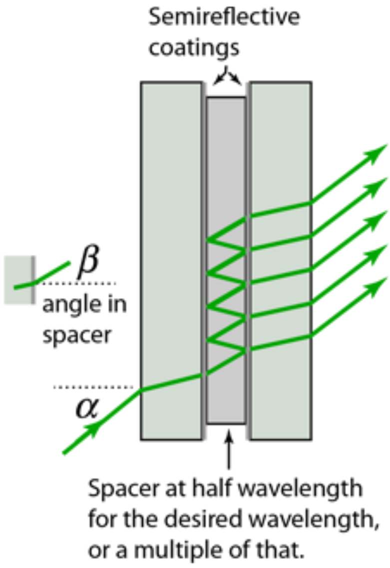


Himawari visible channel

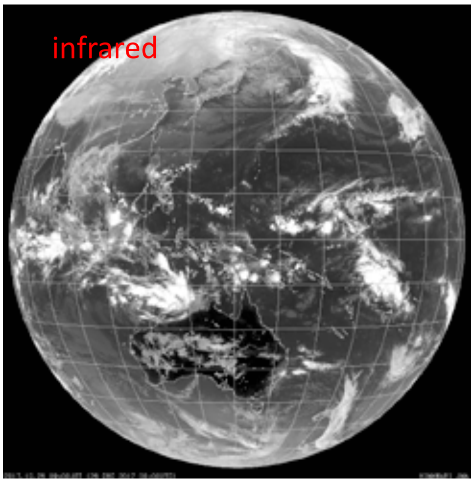
infrared

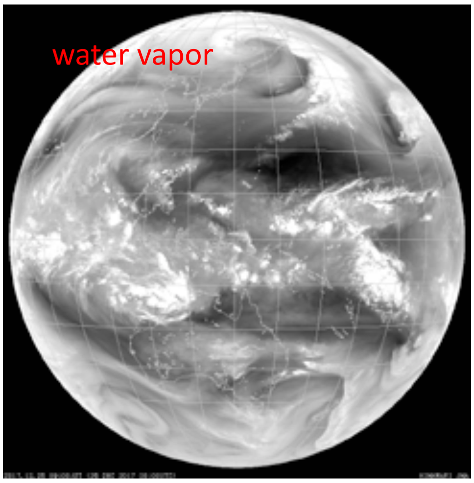
water vapor

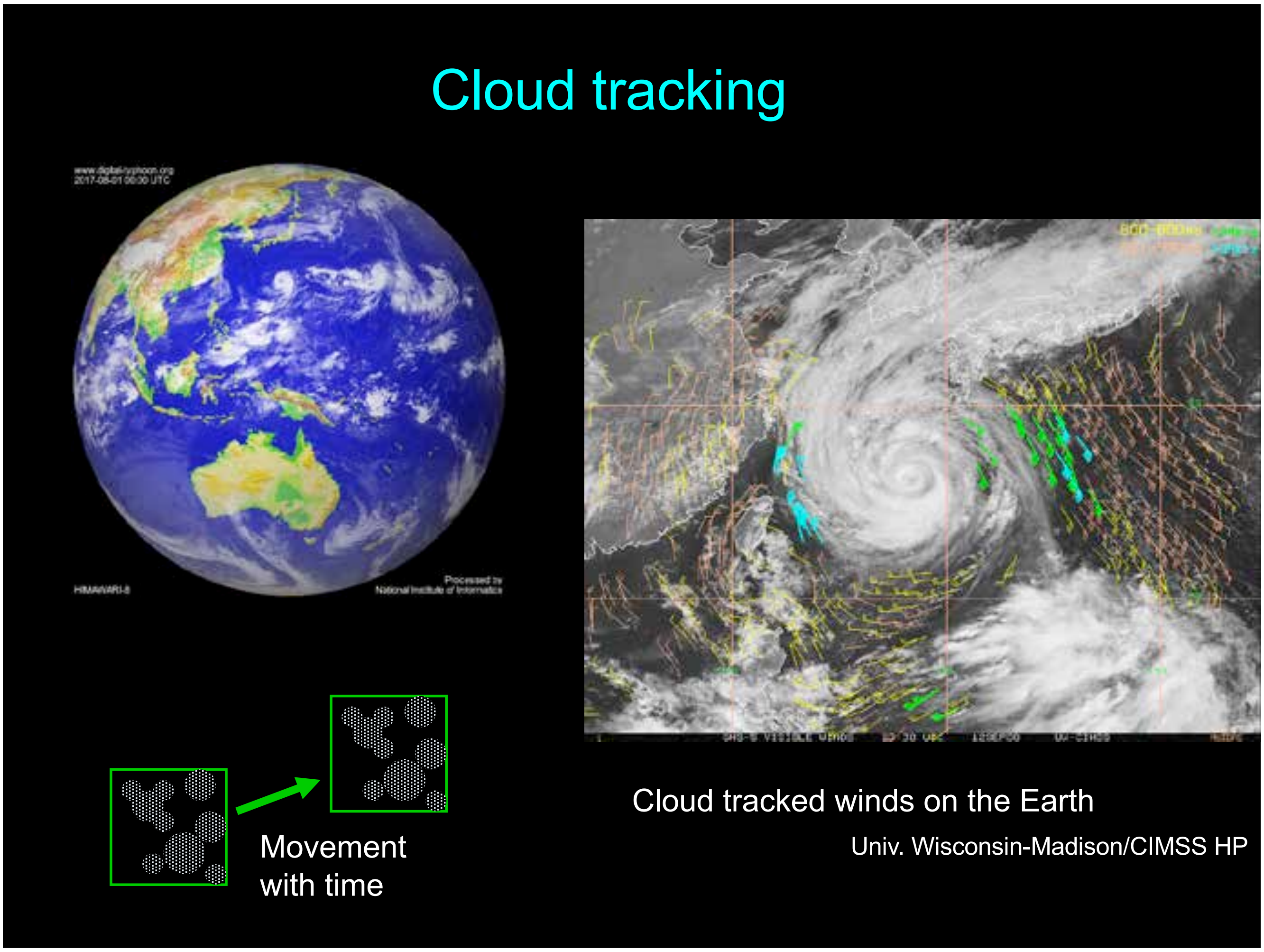
Cloud tracking
www.digital-typhoon.org
2017-08-01 00:00 UTC
HIMAWARI-8
Processed by
National Institute of Informatics
Movement
with time
Cloud tracked winds on the Earth
Univ. Wisconsin-Madison/CIMSS HP

Junocam: Juno's Outreach Camera

Hansen et al. (2014)

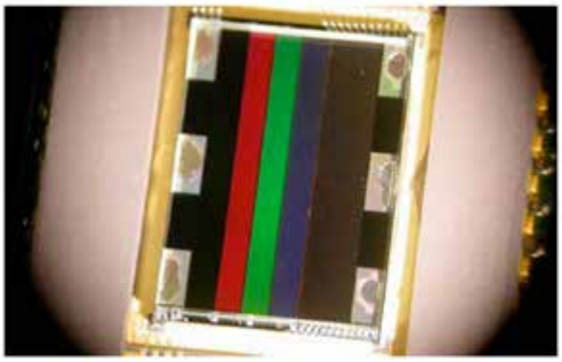

Fig. 12 Color filters are bonded directly to the CCD

Table 3 Junocam filter characteristics

Band	Blue	Green	Red	Methane
Center wavelength	480.1 nm	553.5 nm	698.9 nm	893.3 nm
FWHM	45.5 nm	79.3 nm	175.4 nm	22.7 nm

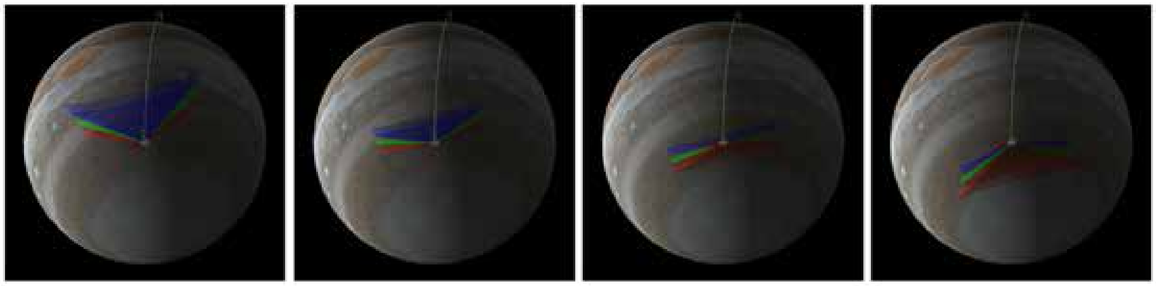

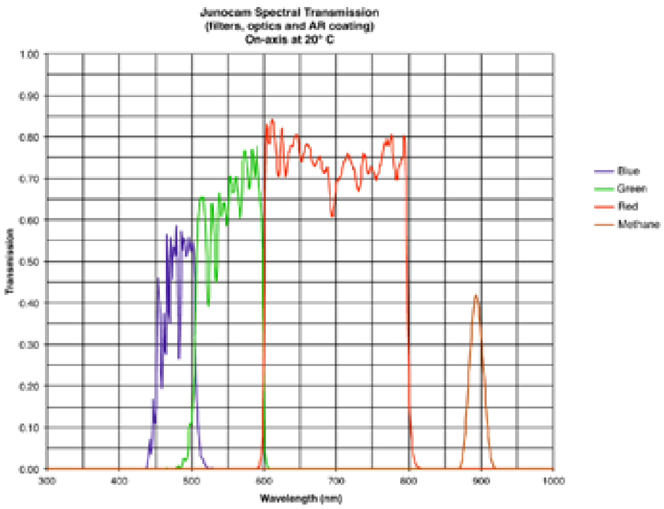

Fig. 13 Bandpasses and transmission are shown for Junocam's four filters

Spectroscopy

Absorption lines

Extinction coefficient

line-shape function

$$k_\nu = \sum_n S_n f_n(\nu - \nu_n)$$

line strength

Andrews (2010)

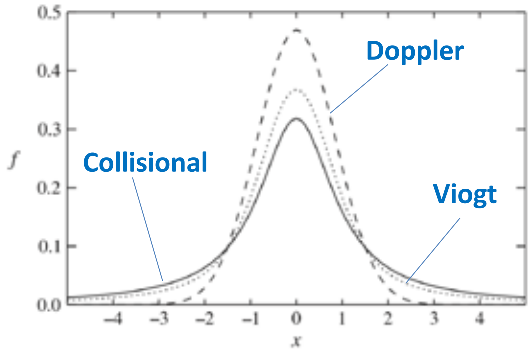

Illustrating the Lorentz (solid), Doppler (dashed) and Voigt (dotted) line shapes as a function of $x = (\nu - \nu_0)/\alpha$, where α is the half-width at half maximum appropriate for each shape. The curves are normalised such that the area under each is the same.

Collisional broadening

$$f(\nu - \nu_n) = \left(\frac{\gamma_L}{\pi}\right) \frac{1}{(\nu - \nu_n)^2 + \gamma_L^2}$$

$$\gamma_L \propto p\, T^{-1/2}$$

Dominant in the lower atmosphere

Doppler broadening

$$k_\nu = \frac{S}{\gamma_D \sqrt{\pi}} \exp\left(-\frac{(\nu - \nu_0)^2}{\gamma_D^2}\right)$$

$$\gamma_D = \frac{\nu_0}{c} \left(\frac{2 k_B T}{m}\right)^{1/2}$$

Dominant in the upper atmosphere

Grating spectrometer

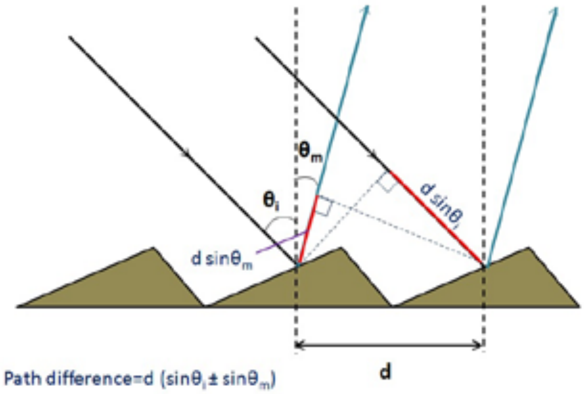

From Wikipedia

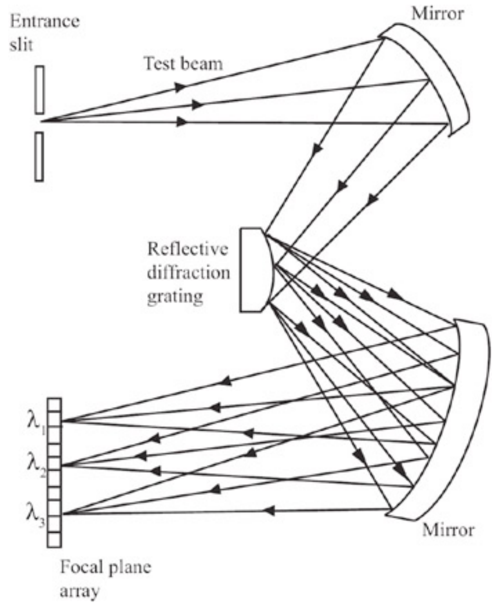

Crawford (2007)

Fourier spectrometer

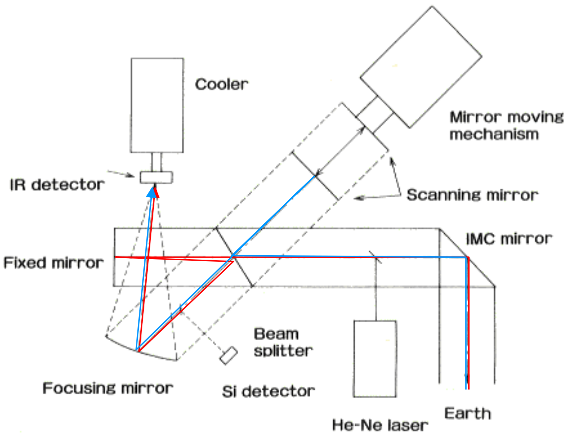

ADEOS/IMG Optical System

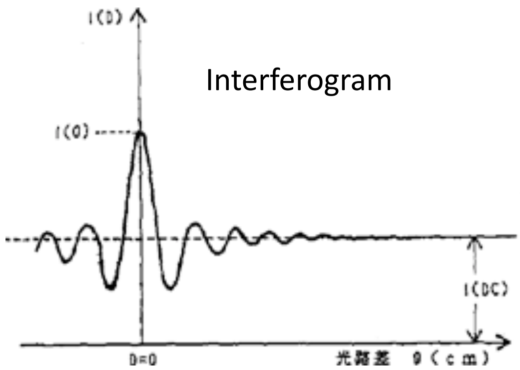

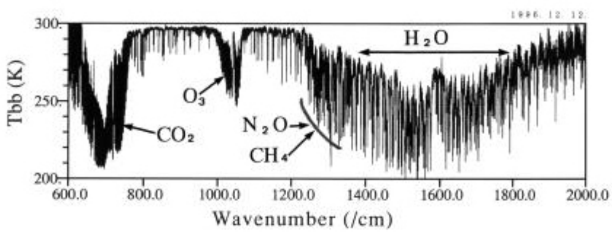

Interferogram →(FFT)→ Spectrum

Retrieval of vertical structures from nadir-looking infrared spectra

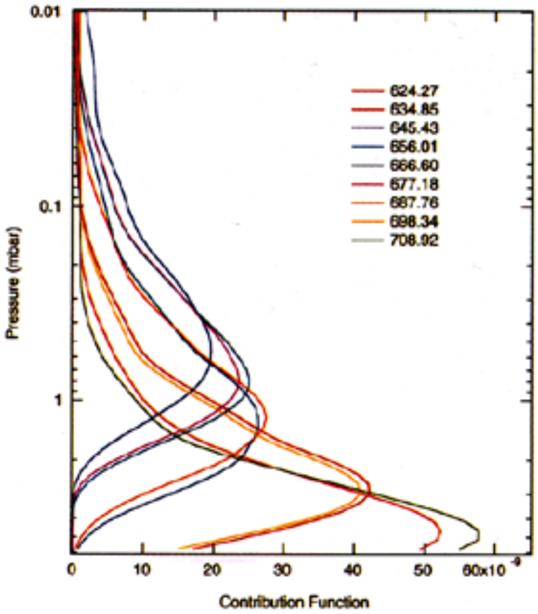

Contribution functions for wavelengths in CO_2 15 µm band for Mars atmosphere

(Conrath et al. 2000)

Outgoing radiance:

$$I = B(T_S)\exp(-\tau_s) + \int_0^{\tau_s} B(T(\tau))\exp(-\tau)\,d\tau$$

$$= B(T_s)\exp(-\tau_s) + \int_0^{\infty} B(T(z))\,k_a(z)\exp(-\tau(z))\,dz$$

$$\tau = \int_z^{\infty} k_a\,dz$$

I：radiance(J/m2/s/str/Hz)
B：Planck function
τ：optical thickness
k_a：absorption coefficient
z：altitude

Thermal emission spectra of Mars

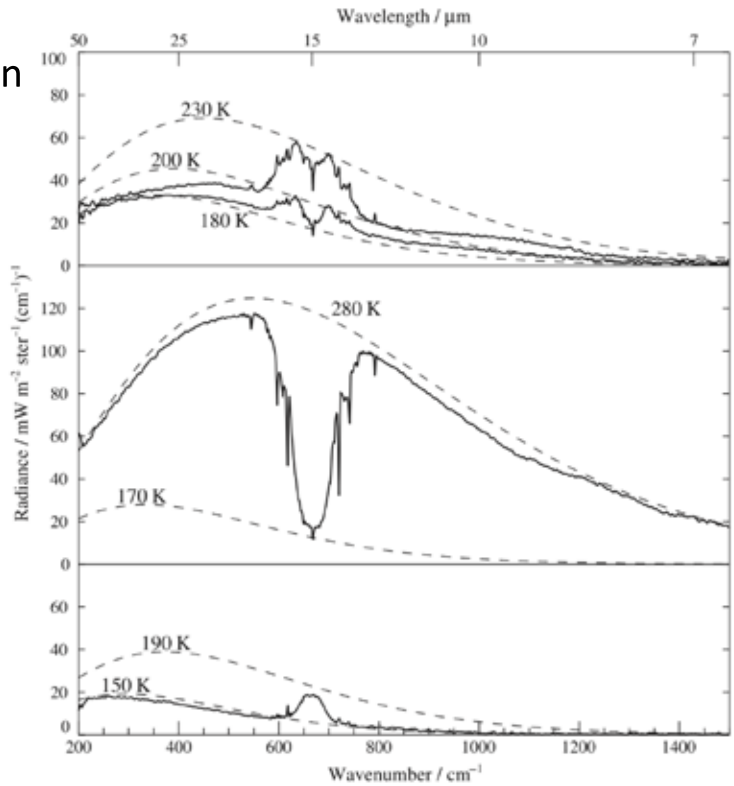

Andrews (2010)

Emission spectra from Mars obtained with the IRIS instrument on Mariner 9 (adapted from Hanel et al. (1972)). Top panel: spectra recorded over the south polar region; upper curve includes a smaller fraction of the polar ice cap than the lower curve. Middle panel: spectrum recorded near 21° S. Lower panel: spectrum recorded near 66° N; note that the condensation temperature of CO_2 at Martian surface pressures is about 145 K. Diagram prepared with the help of Dr S. R. Lewis, using data from the Planetary Data System.

Temperature retrieval from infrared spectra taken by Mars Global Surveyor/TES

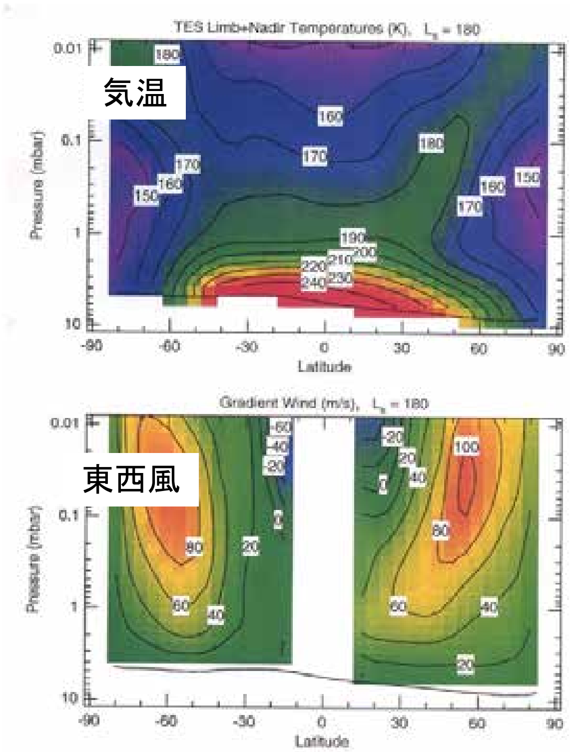

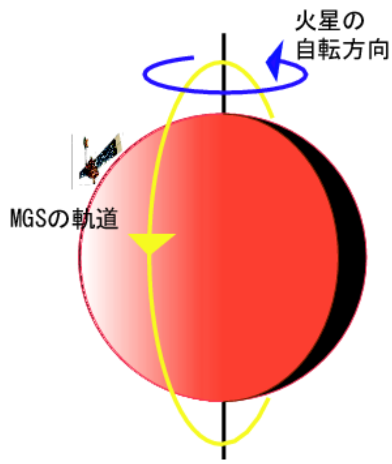

温度風： $\dfrac{\partial u_g}{\partial p} = \dfrac{R}{fp}\dfrac{\partial T}{\partial y}$

Smith et al. (2001)

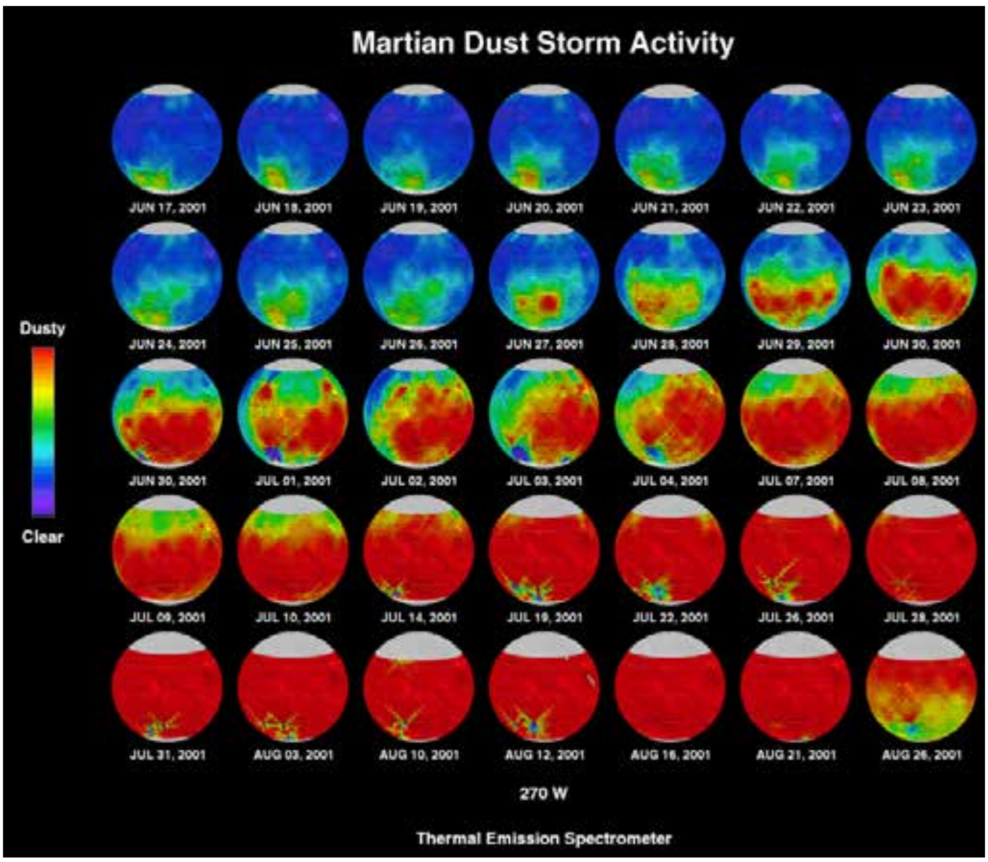

Near-infrared windows of Venus

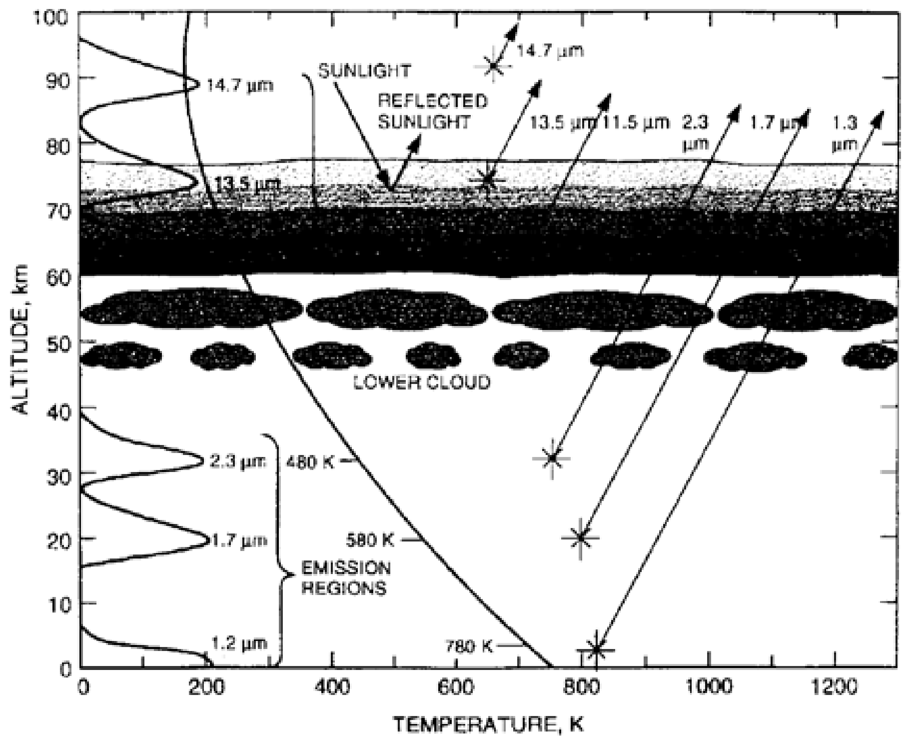

Retrieval of the atmospheric composition of Venus from infrared spectra taken by ground-based telescopes

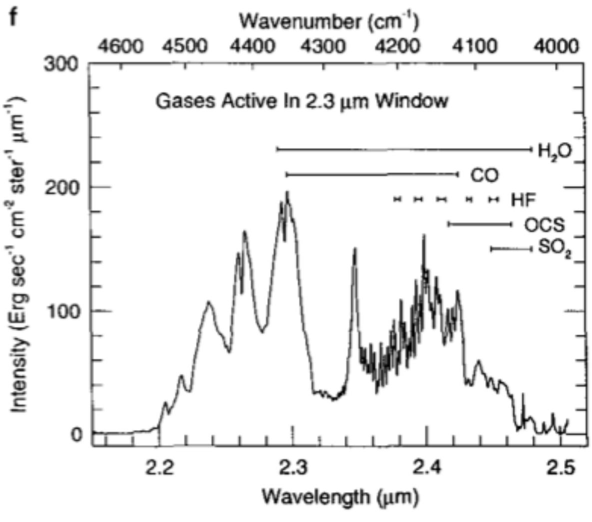

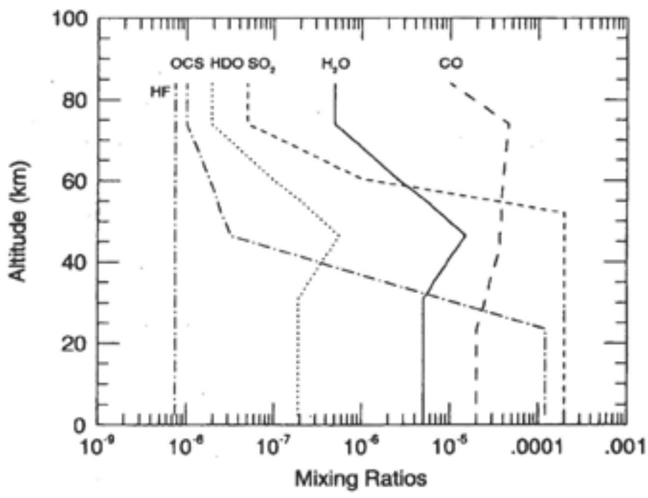

Pollack et al., Icarus 103, 1, 1993

Origin of Venus' clouds

Photochemistry above clouds

Scenario #1 (Net reaction driven by catalytic cycles including ClOx, HOx, NOx)

$$2CO_2 + h\nu \rightarrow 2CO + O_2$$
$$CO + SO_2 + O_2 + h\nu \rightarrow CO_2 + SO_3$$
$$\overline{CO_2 + SO_2 + h\nu \rightarrow CO + SO_3}$$

Scenario #2

$$SO_2 + h\nu \rightarrow SO + O$$
$$SO + h\nu \rightarrow S + O$$
$$SO_2 + O \rightarrow SO_3 \;\; (\times 2)$$
$$\overline{3\,SO_2 + h\nu \rightarrow S + 2SO_3}$$

- SO_3 rapidly reacts with H_2O: $\boxed{SO_3 + H_2O \rightarrow H_2SO_4}$
- Elemental sulfur (S) can serve as condensation nuclei.

Galileo probe (entry: December 7, 1995)

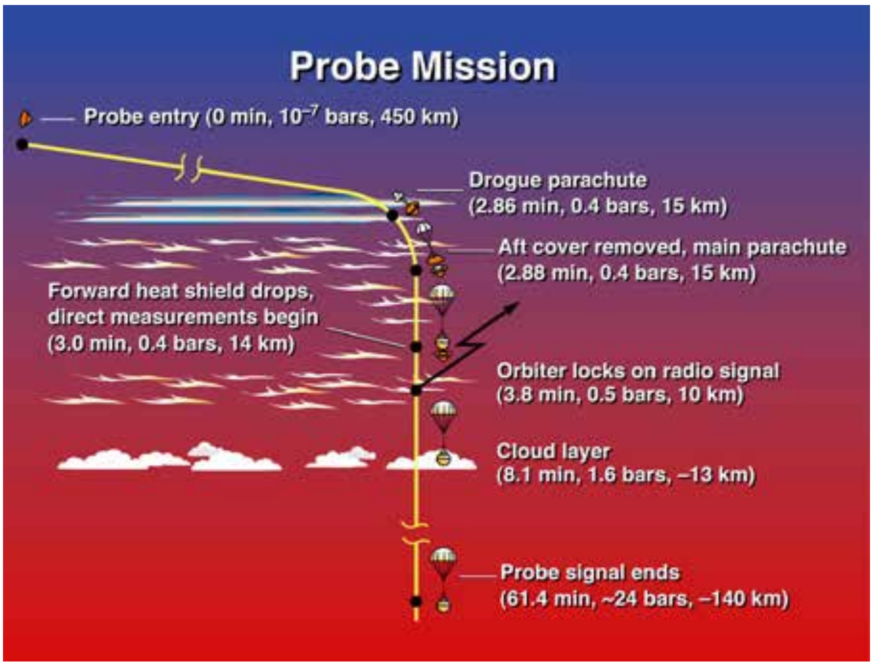

Dry atmosphere ?

- Brightness of the sky abruptly drops off at a pressure level of 0.6 bars, indicating an ammonia cloud layer above this height. The tenuous cloud layer detected by the NEP was *not* seen by this experiment.
- Clouds are patchy and that the Probe went through a relatively clear area. a

- The atmosphere has much less oxygen than the Sun's atmosphere, implying a surprisingly dry atmosphere.
- Planetary scientists had expected oxygen to be enriched relative to the solar value due to impacts by comets and other small bodies over the 4.5 billion years. a

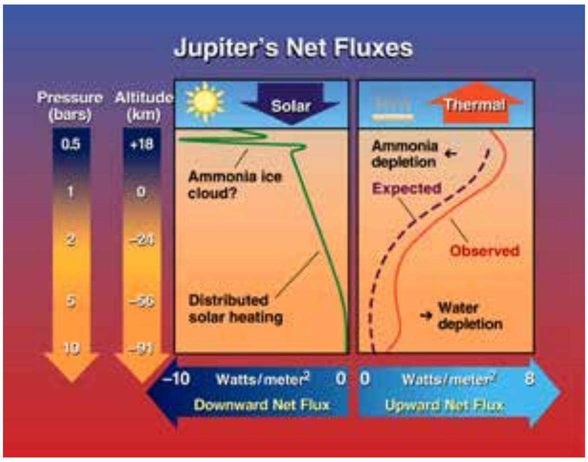

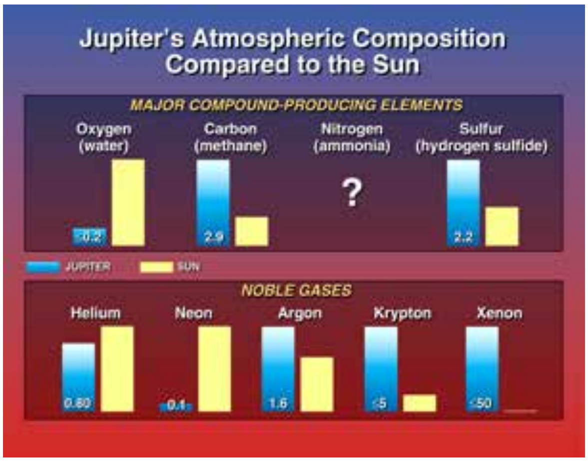

The probe apparently entered a special location

The Probe entry site is near the edge of a so-called infrared "**hot spot**". These "hot spots" are believed to represent regions of diminished clouds on Jupiter.

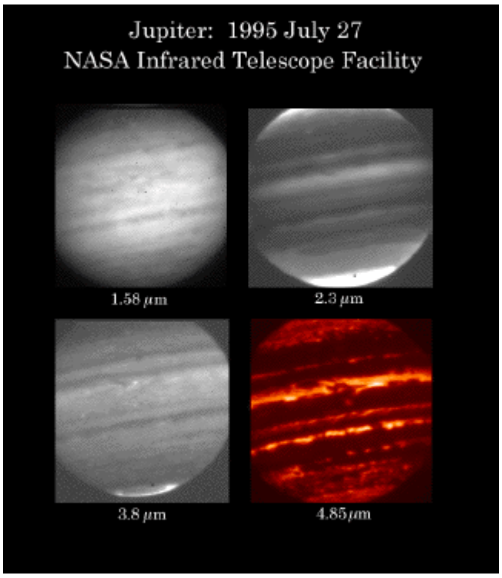

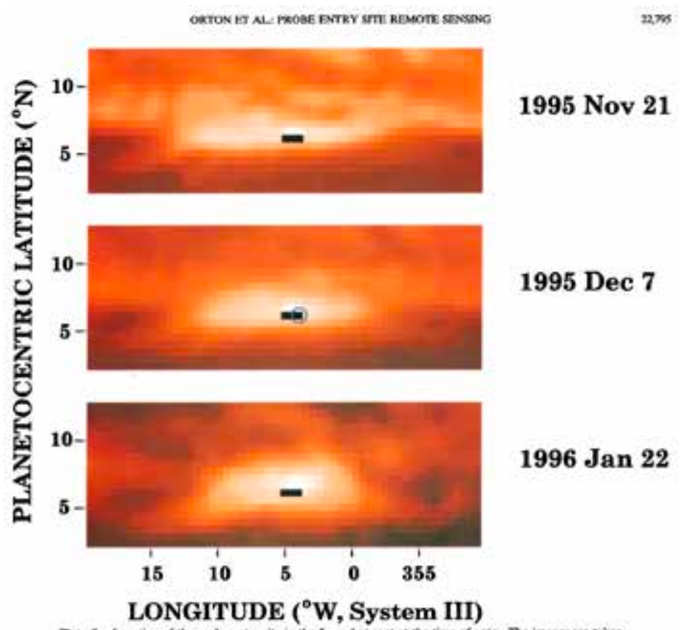

Plate 3. Location of the probe entry site in the 5-μm hot spot at the time of entry. The images are taken from the upper panel of Plate 2 and, again, scaled to the brightest pixel in each image. A single 0.5° × 0.5° pixel is used to denote the 6.5°N planetocentric latitude and System III longitude of the probe entry, and a 1.5° longitude (three-pixel) extent depicts the longitudinal extent of the probe entry path, starting from 350 km above the 1-bar level to the 1-bar level and deeper (as in Figures 1 and 2 of *Orton et al.* [1996]). A 1-σ circle shows the effects of the pointing uncertainty on the location of the final portion of the probe entry. The panels from different dates were aligned together using a drift rate of 103 m/s relative to System III.

Orton et al. 1998

Heating of Jupiter's upper atmosphere above the Great Red Spot

Donoghue et al. (2016, Nature)

- infrared spectroscopy using SpeX spectrometer on the NASA Infrared Telescope Facility (IRTF)
- rotational-vibrational emission lines from H3+, a major ion in Jupiter's ionosphere

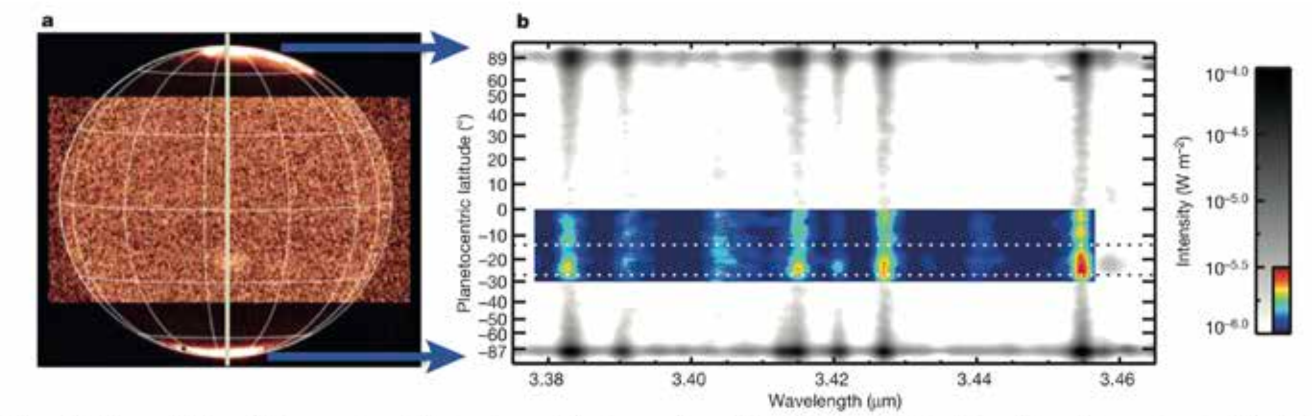

Figure 1 | The acquisition of Jovian spectra. a, Jupiter as observed by the SpeX slit-jaw imager and L-filter (3.13–3.53 μm), on 4 December 2012. Bright regions at the poles result from auroral emissions; the contrast at low and mid-latitudes has been enhanced for visibility. The vertical beige line in the middle of the image indicates the position of the spectrometer slit, which was aligned along the rotational axis. **b**, The co-added spectrum of seven GRS-containing exposures; dotted horizontal lines indicate the latitudinal range of the GRS. Further details are given in the Methods section.

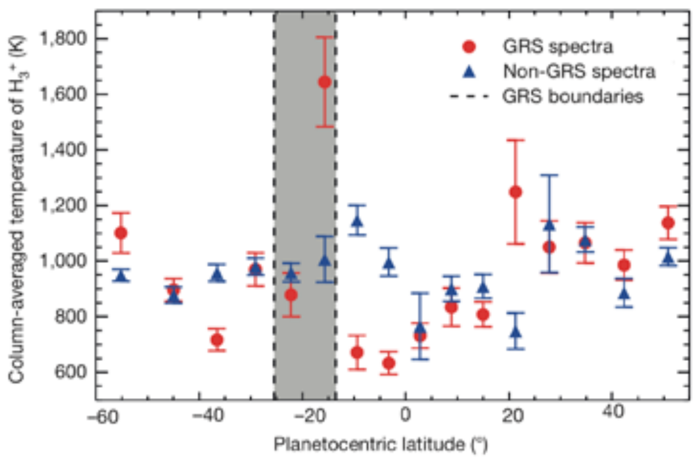

Figure 3 | Jovian H_3^+ temperatures versus planetocentric latitude. Column-averaged temperatures of H_3^+ shown here are each derived from model fits to the discrete H_3^+ emission lines as shown in Fig. 2. Red circle symbols correspond to the co-addition of GRS-related spectra (that is, from the spectral image in Fig. 1b) between 239° and 253° in Jovian system III Central Meridian Longitude (CML). The GRS latitudes are indicated by the grey shading. Blue triangle symbols were derived from exposures taken in the ranges 293°–359° and 0°–82° CML, that is, longitudes well separated from the GRS, representing the 'ordinary' background conditions based on solar heating alone. The modelled temperature of the upper atmosphere for these non-auroral regions is 203 K (ref. 1). Uncertainties are standard errors of the mean.

"This hotspot must be heated from below, and this detection is therefore strong evidence for coupling between Jupiter's lower and upper atmospheres, probably the result of upwardly propagating acoustic or gravity waves."

Jovian thermospheric temperature

Waite et al. (1983)

- Temperature rise across the thermosphere due to solar UV heating is predicted to be <100 K.
- A much stronger source of heat must be present.
  - Precipitating electrons
  - Wave heating (gravity wave, acoustic wave)

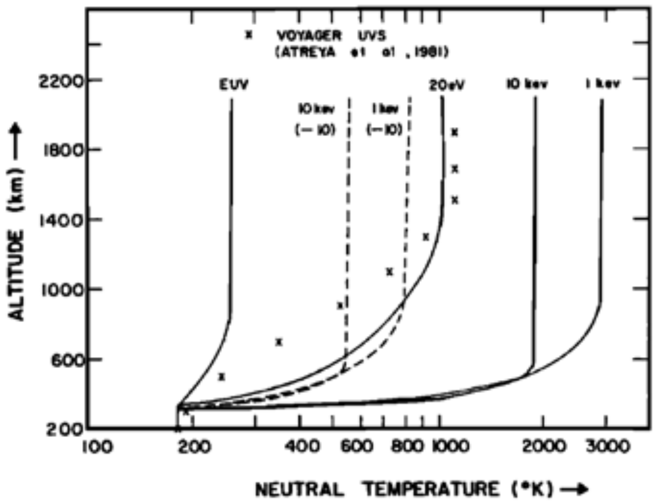

Fig. 16. Neutral temperature as a function of altitude for several cases of interest. The EUV results use only photoelectrons as a heat source. The 20-eV case considers the heating due to 20-eV electrons with an energy flux equal to 0.5 ergs $cm^{-2}s^{-1}$. The 1- and 10-keV auroral electron cases show the effects of electron heating from 1- and 10-keV electrons with an energy flux of 10 ergs cm^{-2} s^{-1} and for auroral heating rates diluted by a factor of 10 to illustrate the possible global effects of auroral heating. The Voyager UVS stellar occultation-derived profile is shown by the crosses.

A map of the day-night contrast of the extrasolar planet HD 189733b (Knutson et al. 2007)

A minimum brightness temperature of 973 +/- 33 K and a maximum brightness temperature of 1212 +/- 11 K at a wavelength of 8 microns, indicating that energy from the irradiated dayside is efficiently redistributed throughout the atmosphere

Observed phase variation for HD 189733b, with transit and secondary eclipse visible.

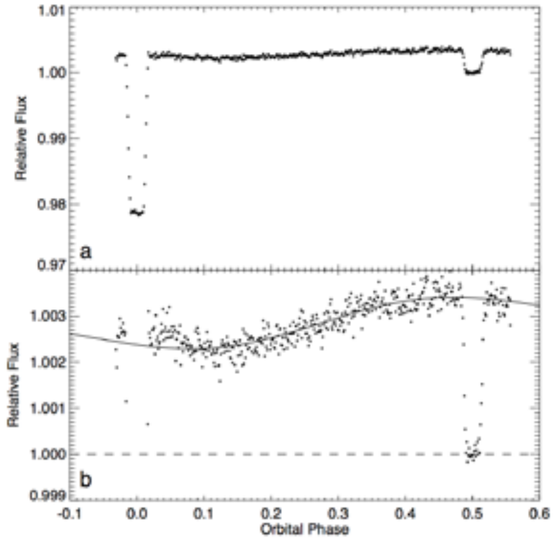

Brightness estimates for 12 longitudinal strips on the surface of the planet

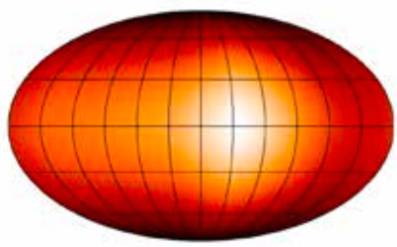

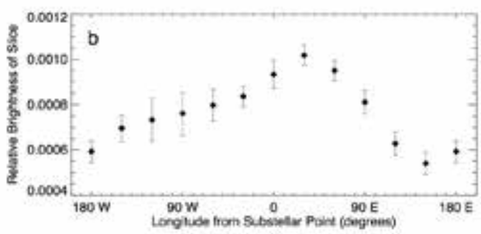

Total ozone mapping spectrometer(TOMS)

6 bands : 308.6, 312.5, 317.5, 322.3, 331.2, 360.0 nm

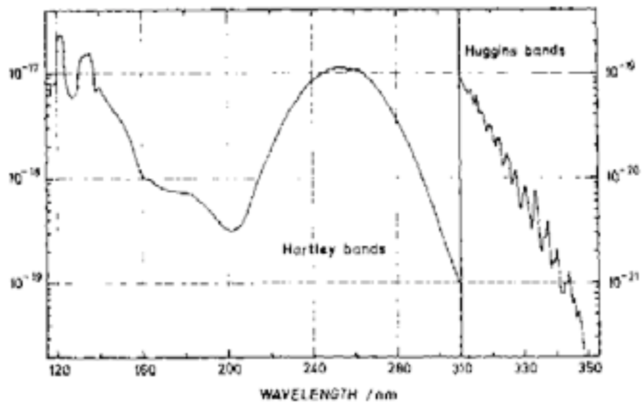

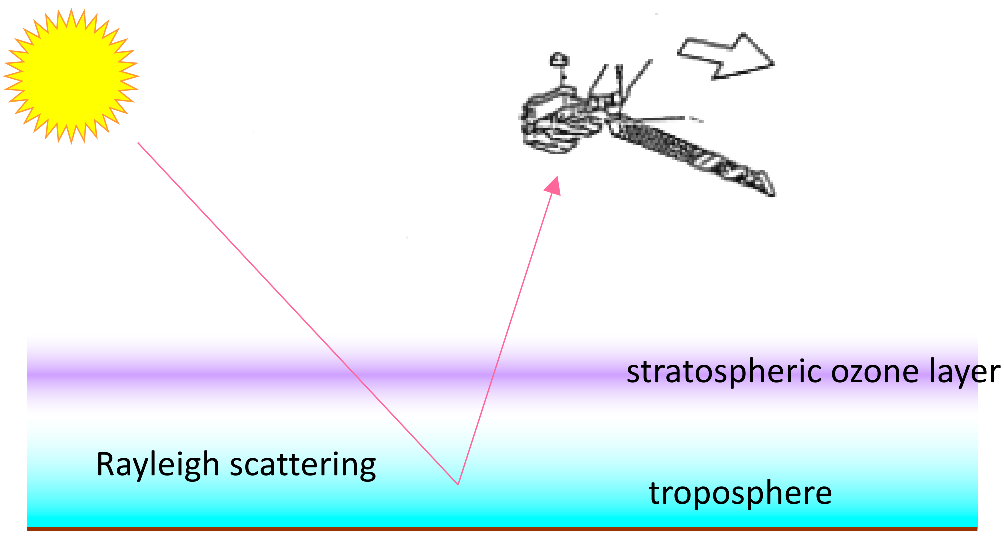

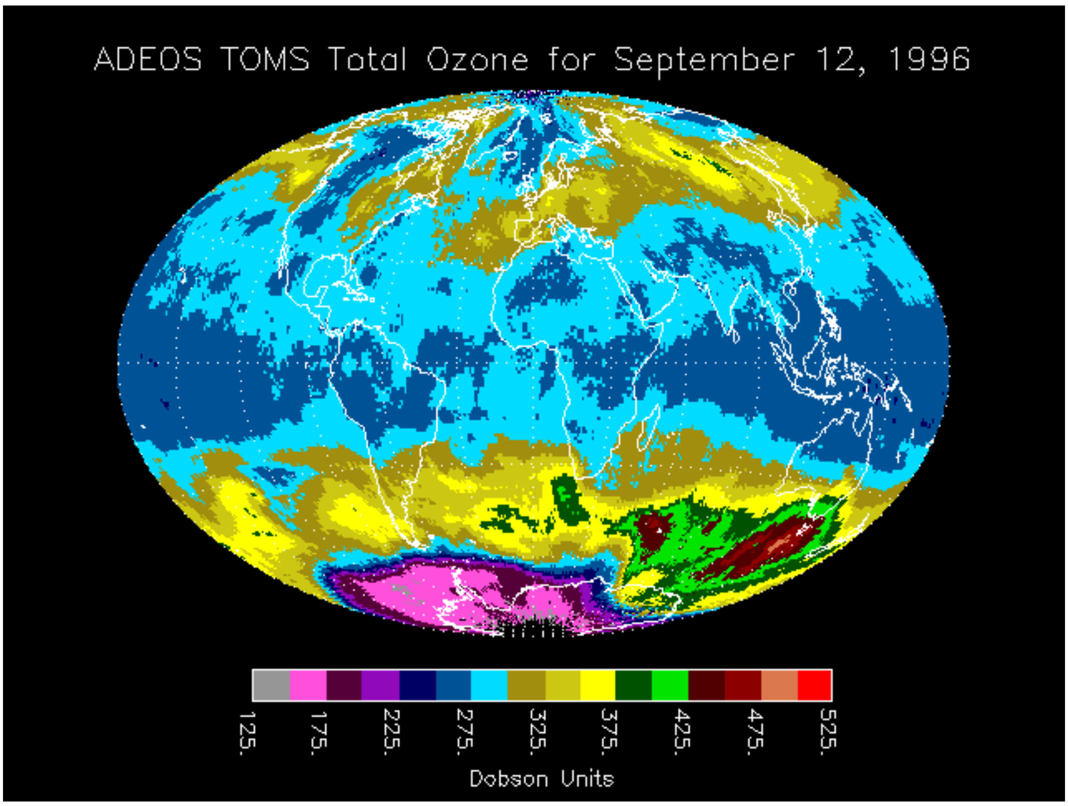

GOSAT
Fourier Transform
Spectrometer

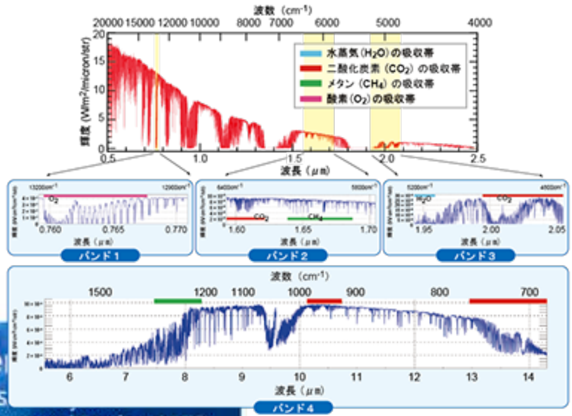

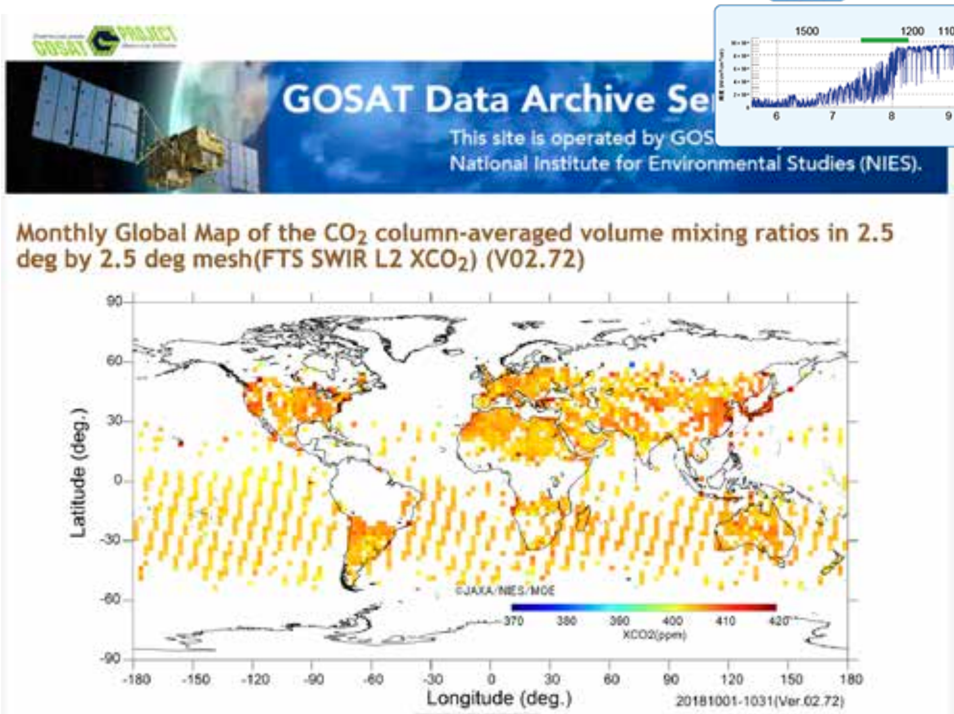

Strong Release of Methane on Mars in Northern Summer 2003

Michael J. Mumma,[1*] Geronimo L. Villanueva,[2,3] Robert E. Novak,[4] Tilak Hewagama,[3,5] Boncho P. Bonev,[2,3] Michael A. DiSanti,[3] Avi M. Mandell,[3] Michael D. Smith[3]

火星メタンの地上分光観測：
軌道運動によるDoppler shiftを利用

Mumma et al. (2009)

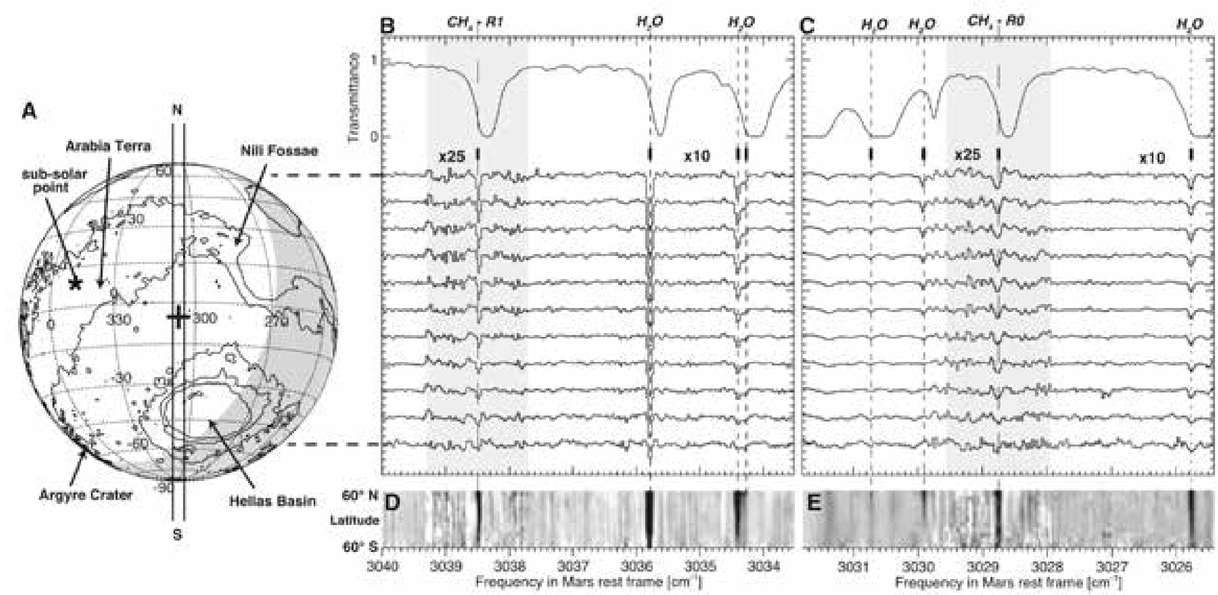

Mumma et al. (2009)

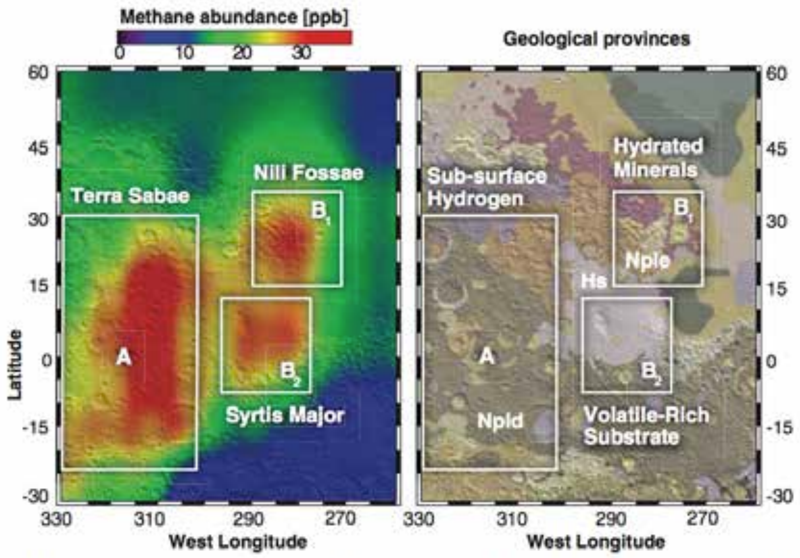

Fig. 3. Regions where CH_4 appears notably localized in northern summer (A, B_1, and B_2) and their relationship to mineralogical and geomorphological domains. **(A)** Observations of CH_4 near the Syrtis Major volcanic district. **(B)** Geologic map of Greeley and Guest (*45*) superimposed on the topographic shaded relief from the Mars Orbiter Laser Altimeter (*46*). The most ancient terrain units are dissected and etched Noachian plains (Npld and Nple) (~3.6 to 4.5 billion years old, when Mars was wet) and are overlain by volcanic deposits from Syrtis Major of Hesperian (Hs) age (~3.1 to 3.6 billion years old).

Martian water vapor: Mars Express PFS/LW observations of thermal infrared emission

Fouchet et al. (2007)

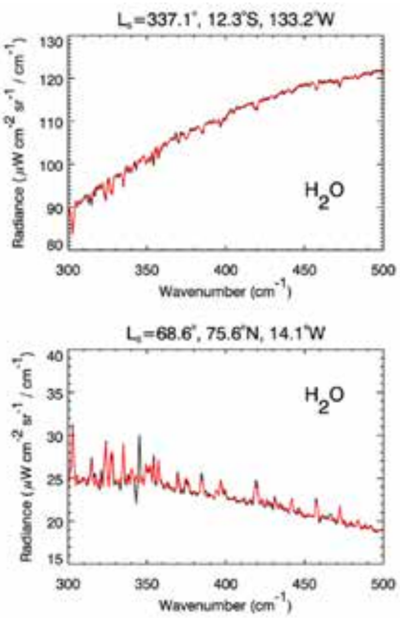

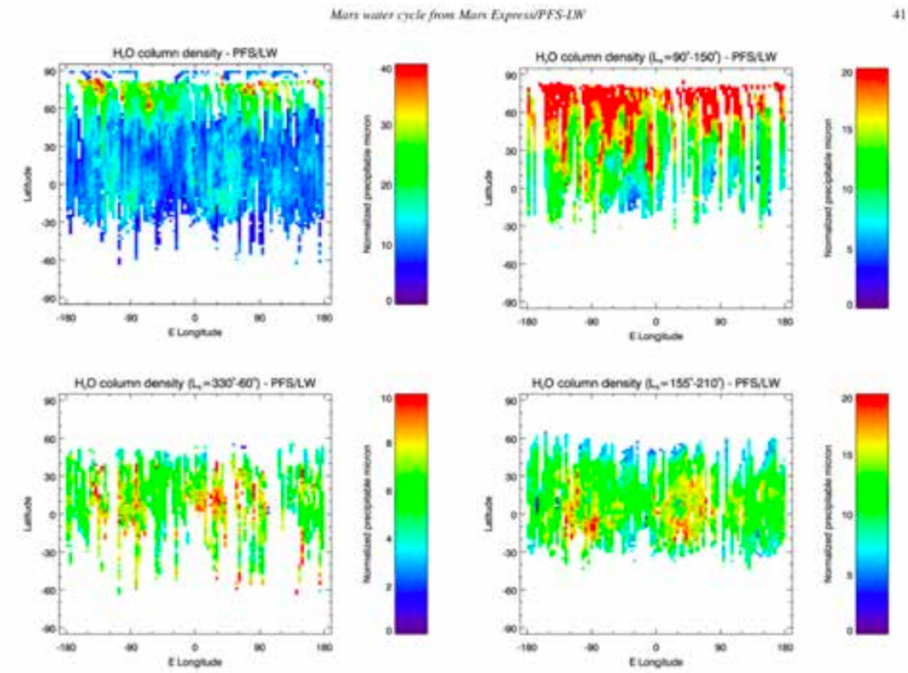

Fig. 6. Geographical distribution of water. Water columns are here normalized to a common 610 Pa pressure. Top left: entire dataset. Top right: $L_s = 330°–60°$. Bottom left: $L_s = 90°–150°$. Bottom right: $L_s = 155°–210°$.

Doppler wind measurements of the Venusian thermosphere from sub-millimeter CO absorption line observations
Clancy et al. (2012)

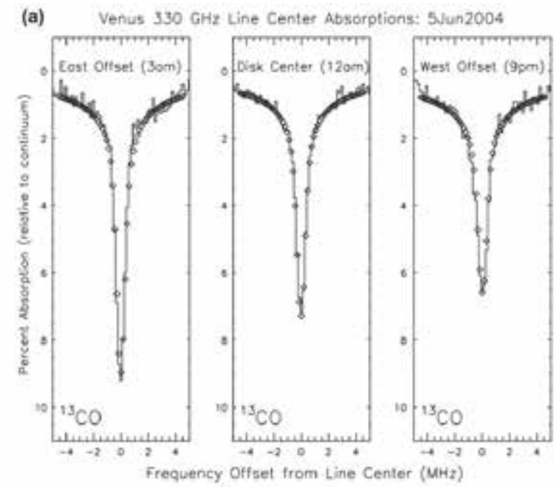

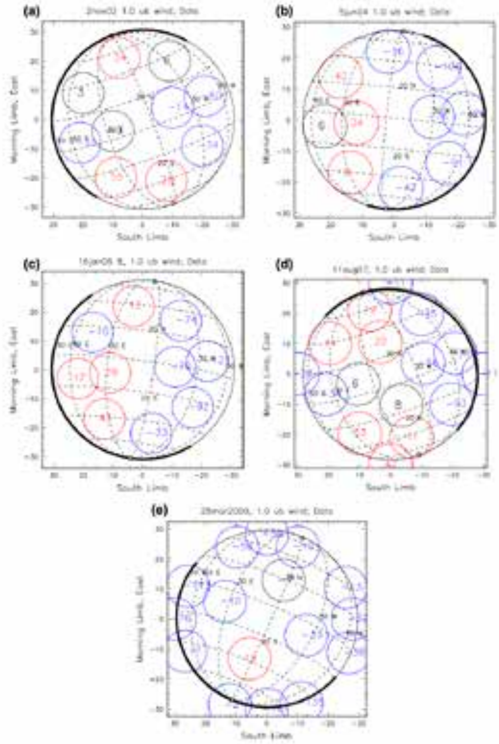

Fig. 7. The distribution and amplitude of fitted Doppler wind velocities (m/s) at the 1 μbar pressure level (~109 km altitude) are indicated for beam integration positions across the nightside apparent disk at Venus inferior conjunctions on November 2, 2002 (a), June 5, 2004 (b), January 16, 2006 (c), August 11, 2007 (d), and March 28, 2009 (e). Negative (blue) values refer to approaching Doppler winds, positive (red) values refer to receding Doppler winds. Values falling within the 1σ measurement uncertainty (10 m/s at 1 μbar) are indicated by black circles. The diffraction FWHM resolution of each observation is indicated by the circles (14 arcsec). Relatively weak nightside lower thermospheric wind velocities, poorly described by SSAS or zonal circulation, are apparent in (a). Nightside wind velocities consistent with retrograde zonal and SSAS circulation are apparent in (b). Complex zonal and SSAS circulation is apparent in (c) and (d), versus primarily SSAS circulation in (e). (For interpretation of the references to color in this figure legend, the reader is referred to the web version of this article.)

Limb sounding of Earth's stratosphere : ISS/SMILES

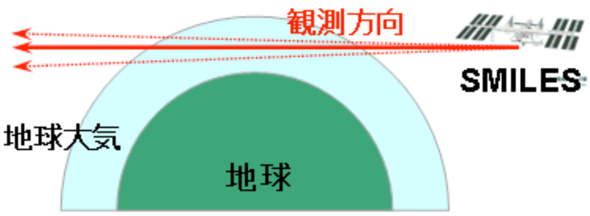

spectroscopy of far-infrared emission

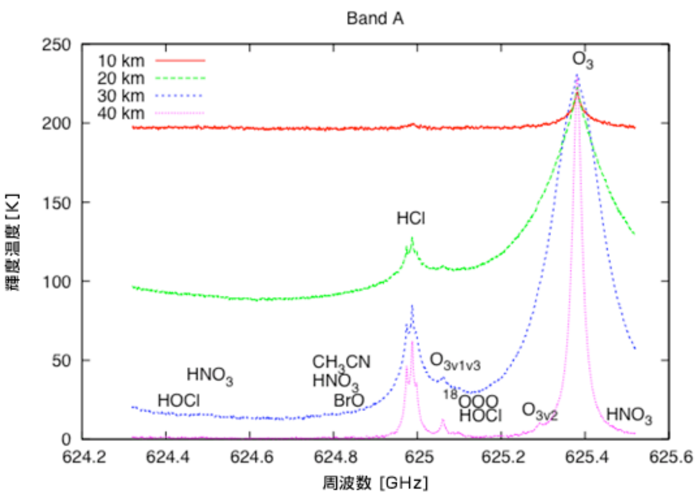

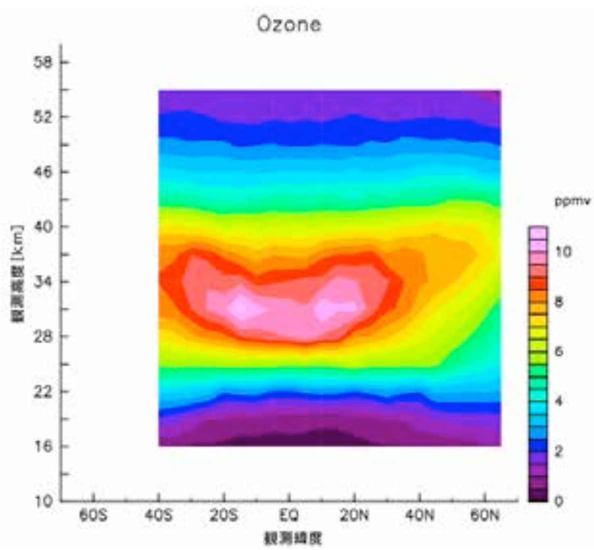

Stellar occultation : Venus Express/SPICAV

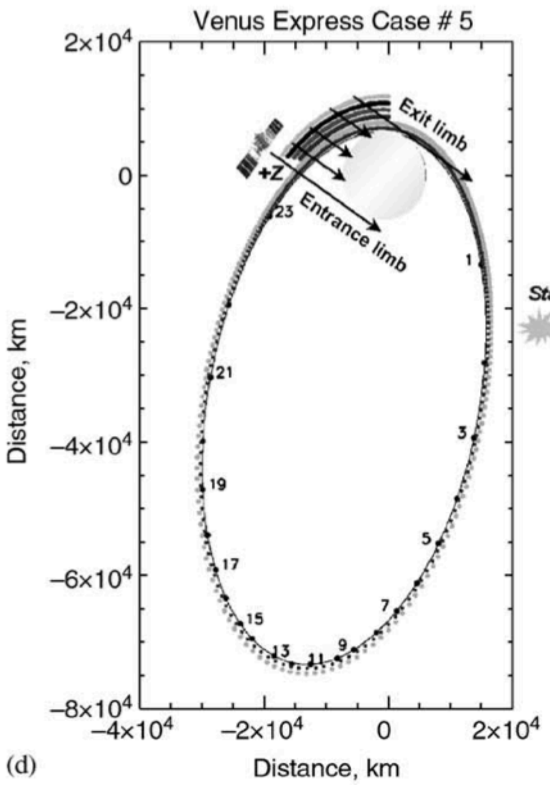

Using stars as the light source

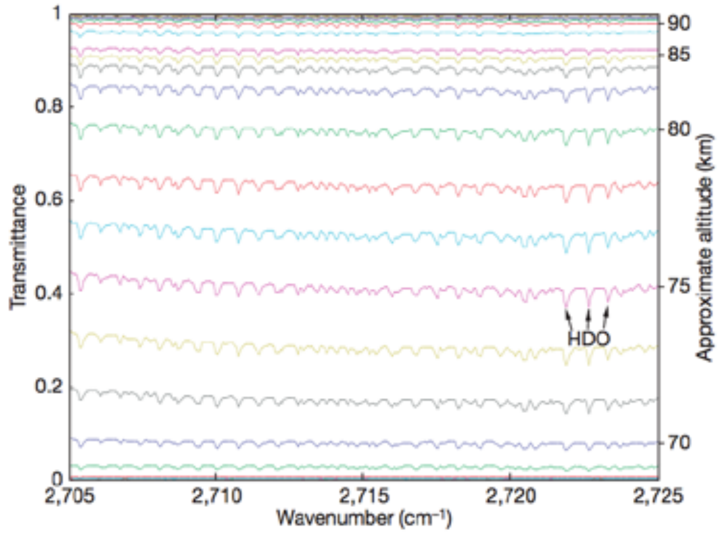

Figure 2 | Typical evolution of atmospheric spectral transmittances through one solar occultation observed by SOIR spectrometer. It is obtained by

Venus Express/SPICAV

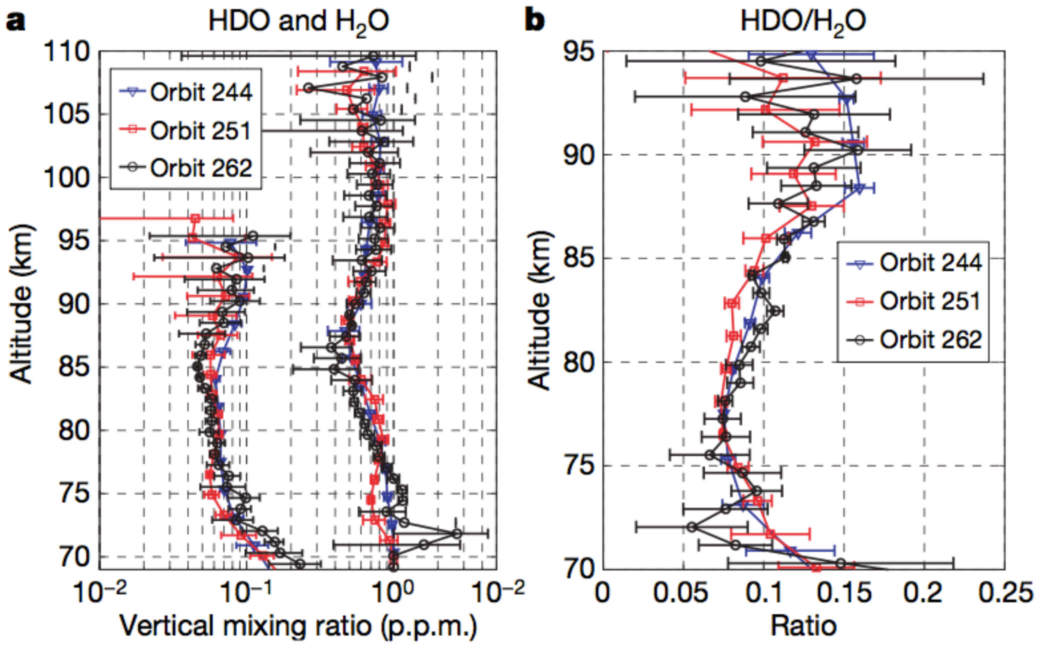

Figure 4 | HDO and H_2O mixing ratio, HDO/ H_2O vertical profiles. Both

Venus Express/SPICAV

Venus' haze layer above clouds

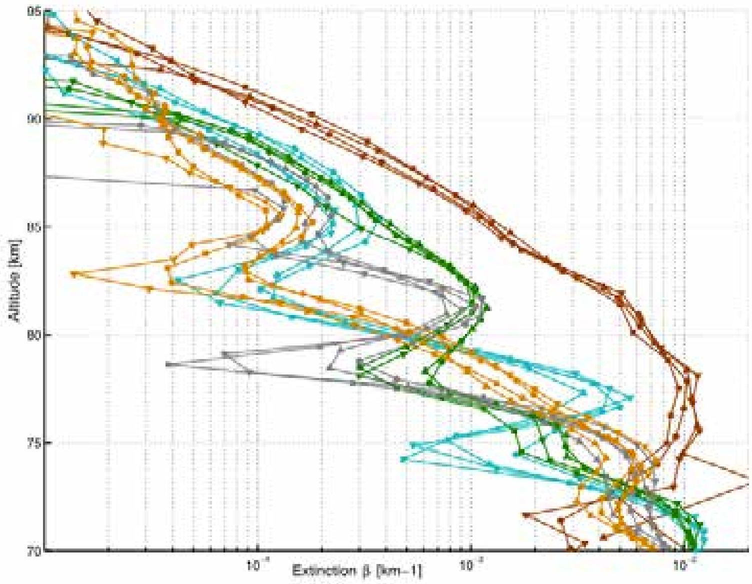

Wilquet et al. (2009)

SO, SO_2 profiles above cloud observed by Venus Express solar occultations (Belyaev et al. 2011)

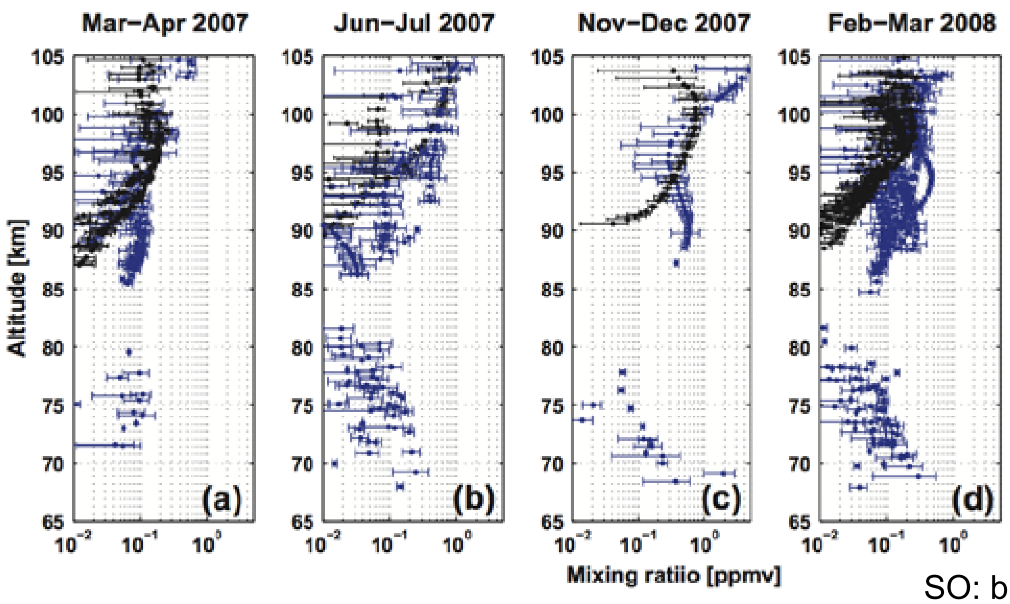

SO: black
SO_2: blue

- Enhancement at high altitudes cannot be explained by traditional photochemical models.

Mars Climate Sounder on Mars Reconnaissance Orbiter

McCleese et al. (2007)

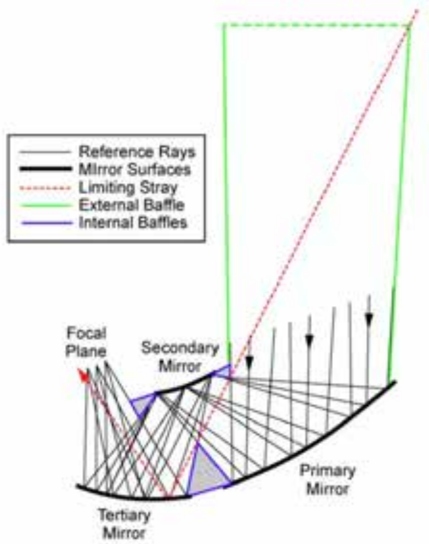

Figure 4. MCS telescope optical schematic and baffle approach.

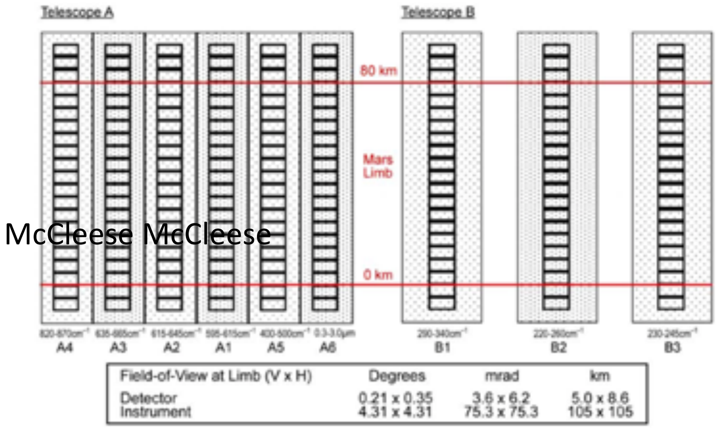

Figure 3. MCS fields of view projected at the limb of Mars. The telescope A and B FOV responses are aligned to be superimposed within one-half FOV in the horizontal dimension and one-tenth FOV in the vertical (shown separated in figure for clarity).

Fast, localized dust storms : key to understand dust lifting and anomalous dust distribution

Meridional cross section of dust mixing ratio

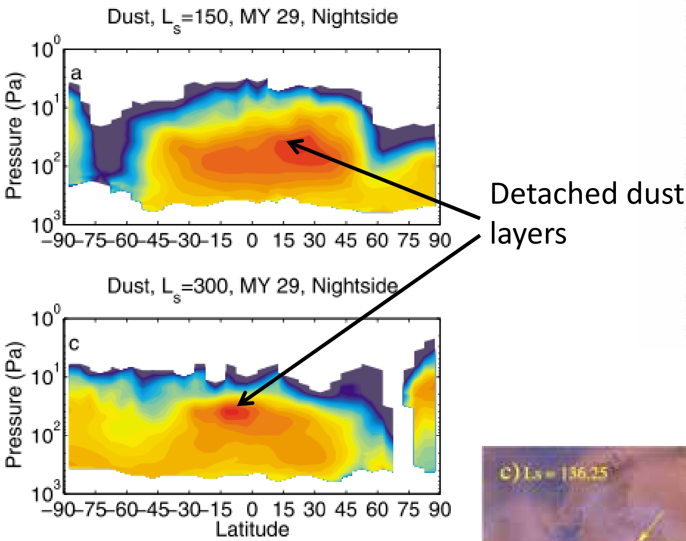

Heavens et al. (2011)

“Rocket dust storm”: source of high-altitude dust ?

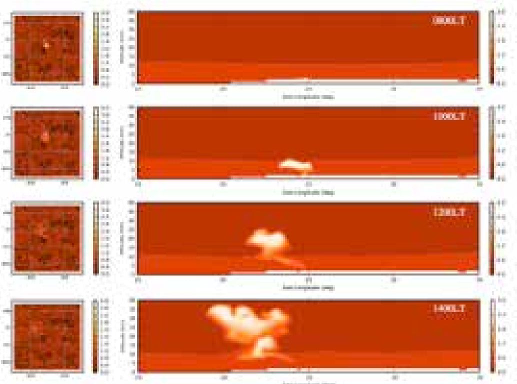

Spiga et al. (2013)

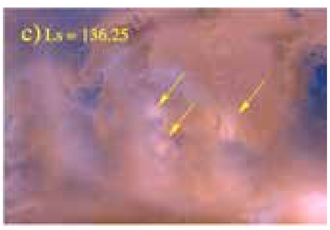

Previous observations failed to detect temporal development of localized dust plumes that might play crucial roles in distributing the background dust

"Limb-viewing" spectroscopy of exoplanets

- Transit spectroscopy

Kreidberg (2018)

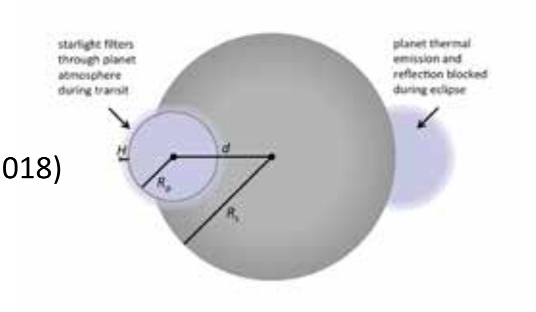

Howe & Burrows (2018)

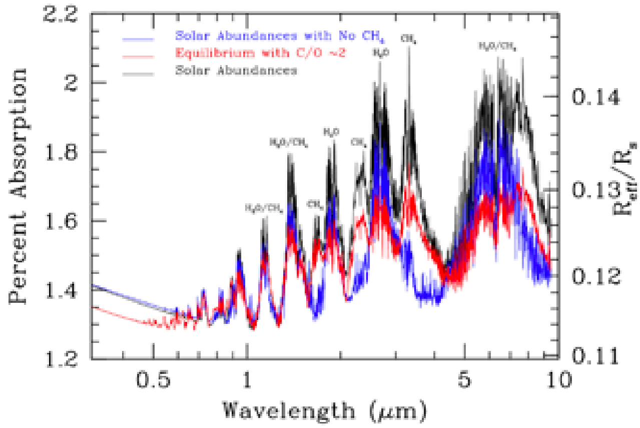

hydrogen-rich atmospheres with non-solar relative abundances

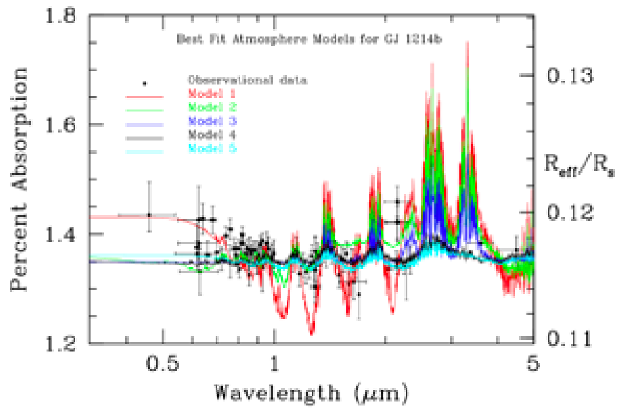

Models 1-3 use a solar-abundance atmosphere, while Models 4 and 5 use an atmosphere of 1% H_2O and 99% N_2

Meadows et al. (2018)
ASTROBIOLOGY, Vol 18

FIG. 6. Transit transmission spectra of potential planetary environments with different O_2 abundances for planet orbiting the M5.5V star Proxima Centauri (Meadows *et al.*, 2018). Illustrating spectral features that can help distinguish photosynthetic from abiotically generated O_2 in a planetary atmosphere. From top to bottom: self-consistent Earth-like atmosphere with 50% cloud cover (21% O_2); 10 bar abiotic O_2 (95% O_2) atmosphere produced by early ocean loss with ocean remaining (purple) and desiccated (orange); 1 bar desiccated $CO_2/CO/O_2$ atmosphere that has reached a kinetic–photochemical equilibrium between the photolysis rate of CO_2 and kinetics-limited recombination (15% O_2). Effective atmospheric radius in kilometers is on the left *y* axes and transit depth is shown on the right *y* axes. The photosynthetic source for O_2 in the Earth-like case is made more likely by the presence of O_2/O_3, water, and methane. High O_2 cases with and without water are distinguished by the presence of O_4, and the behavior of the 0.5–0.7 μm Chappuis band that is sensitive to tropospheric O_3, which is more abundant in the desiccated case. The desiccated chemical equilibrium atmosphere is easily distinguished by its high levels of CO.

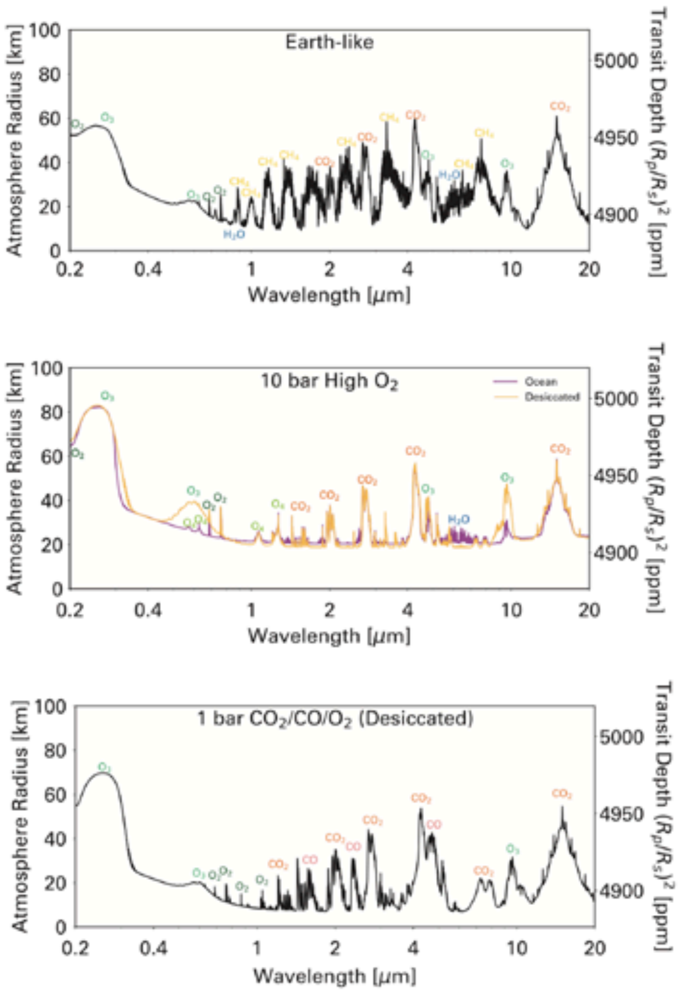

Missions

Venus orbiter AKATSUKI

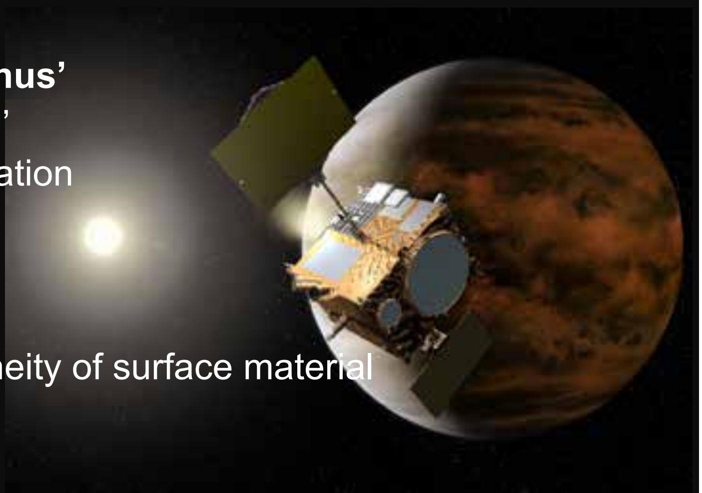

- Science target : **‘Weather of Venus’**
  - Mechanism of ‘super-rotation’
  - Structure of meridional circulation
  - Meso-scale processes
  - Formation of clouds
  - Lightning
  - Active volcanism, inhomogeneity of surface material
- Science instruments
  - 1μm Camera (IR1)
  - 2μm Camera (IR2)
  - Longwave IR Camera (LIR)
  - Ultraviolet Imager (UVI)
  - Lightning and Airglow Camera (LAC)
  - Ultra-stable oscillator (USO)
- Launch: May 2010   Arrival: Dec 2015

Onboard instruments

Instrument	FOV	Detector	Filters	Width	Targets
1-μm Camera **IR1**	12°	Si-CSD/CCD 1024 x 1024 pix	1.01 μm (night)	0.04 μm	Surface, Clouds
			0.97 μm (night)	0.04 μm	H_2O vapor
			0.90 μm (night)	0.03 μm	Surface, Clouds
			0.90 μm (day)	0.01 μm	Clouds
2-μm Camera **IR2**	12°	PtSi-CSD/CCD 1024 x 1024 pix	1.735 μm (night)	0.04 μm	Clouds, Particle size
			2.26 μm (night)	0.06 μm	
			2.32 μm (night)	0.04 μm	CO below clouds
			2.02 μm (day)	0.04 μm	Cloud-top height
			1.65 μm (cruise)	0.3 μm	Zodiacal light
UltraViolet Imager **UVI**	12°	Si-CCD 1024 x 1024 pix	283 nm (day)	15 nm	SO_2 at cloud top
			365 nm (day)	15 nm	Unknown absorber
Longwave IR Camera **LIR**	12.4X 16.4 °	Bolometer 248 x 328 pix	10 μm (day/night)	4 μm	Cloud-top temperature
Lightning & Airglow Camera **LAC**	16°	8 x 8 APD (50kHz sampling in lightning mode)	777.4 nm (night)	4.2 nm	OI lightning
			552.5 nm (night)	4.7 nm	O_2 HerzbergII ariglow
			557.7 nm (night)	3.1 nm	OI airglow
			630.0 nm (night)	3.5 nm	OI airglow
Ultra-stable oscillator for Radio Science **RS**			X-band (8.4GHz)		Vertical prifiles of T, H_2SO_4 (g), Ne

'Near-infrared window of Venus'

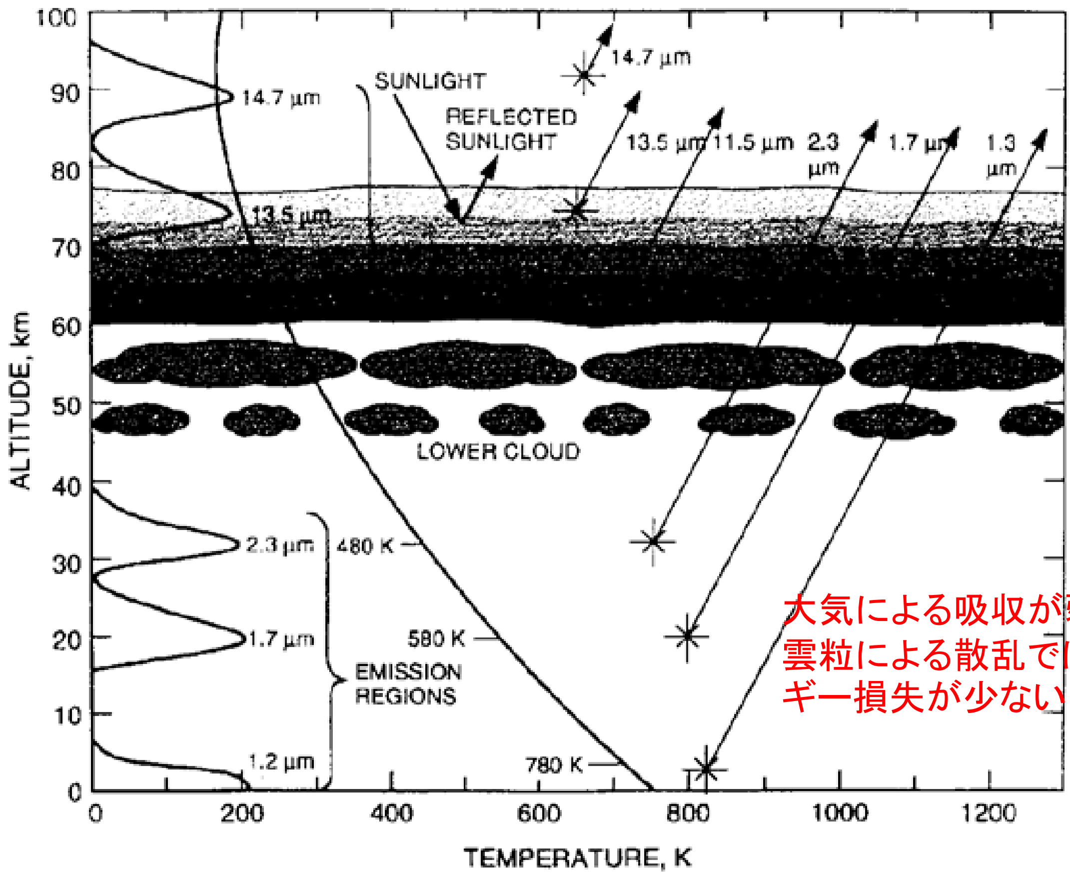

大気による吸収が弱い
雲粒による散乱ではエネルギー損失が少ない（多重散乱）

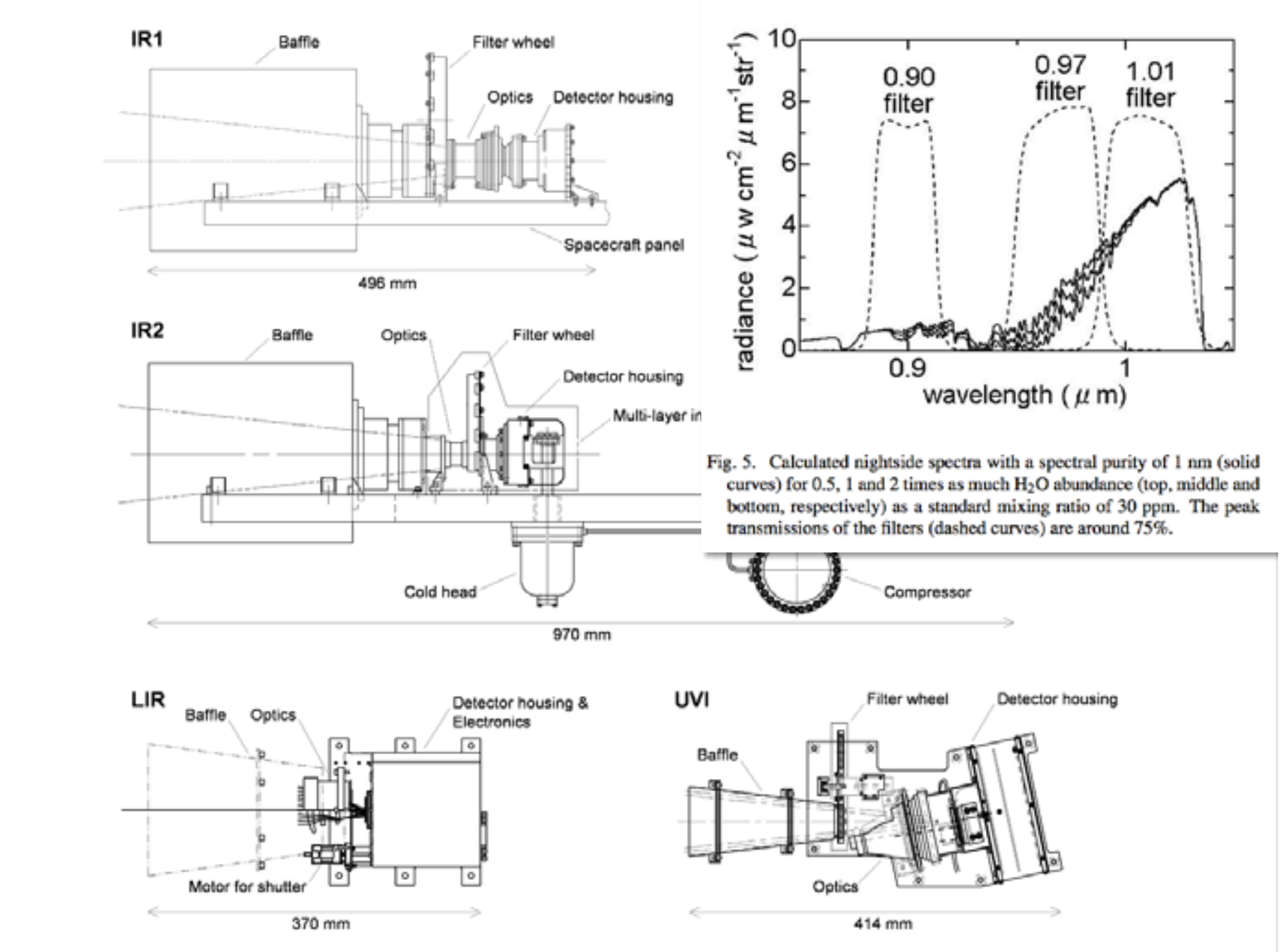

Fig. 5. Calculated nightside spectra with a spectral purity of 1 nm (solid curves) for 0.5, 1 and 2 times as much H_2O abundance (top, middle and bottom, respectively) as a standard mixing ratio of 30 ppm. The peak transmissions of the filters (dashed curves) are around 75%.

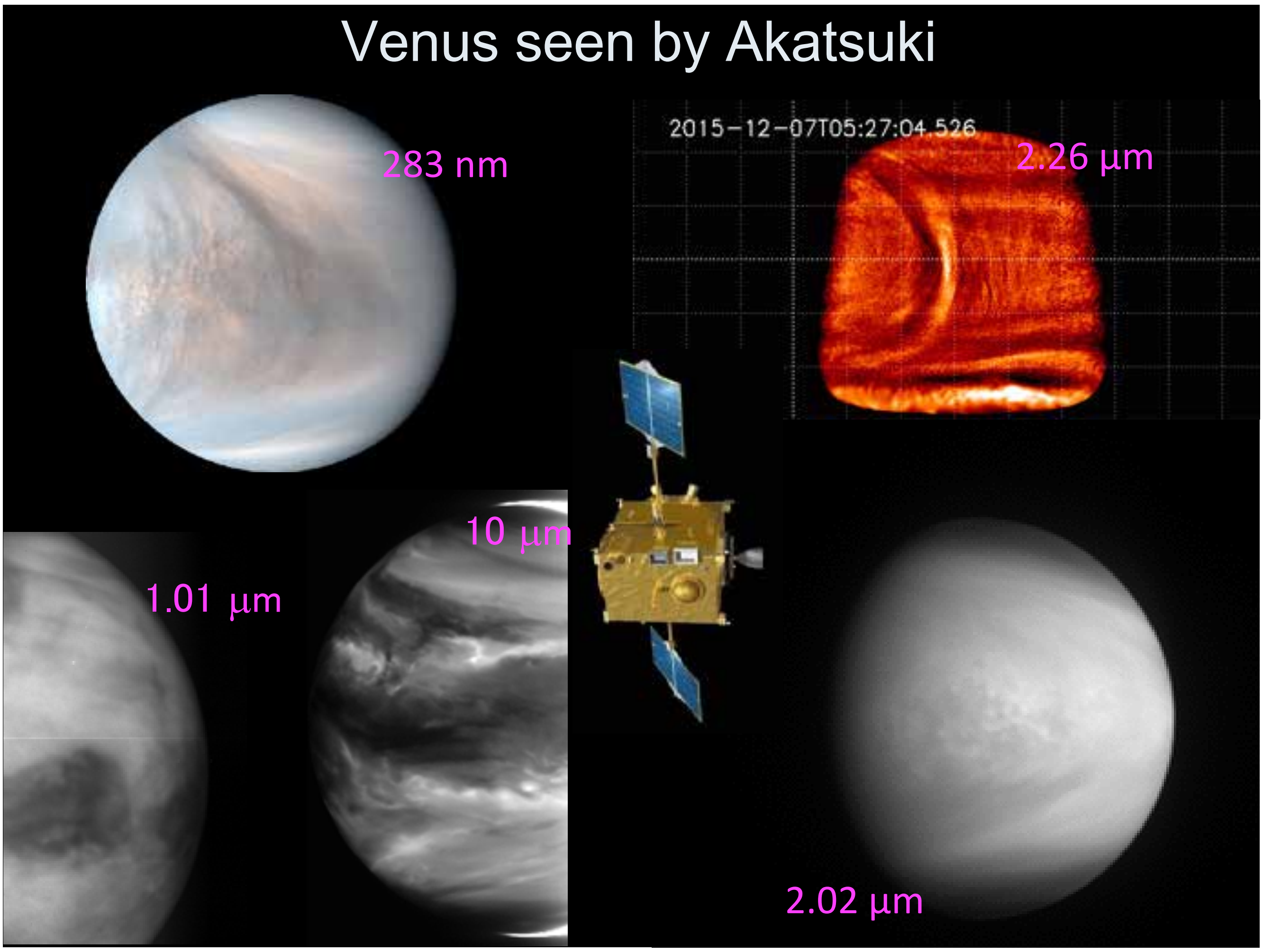

Atmospheric thermal tides observed by Akatsuki

Cloud temperature deviation

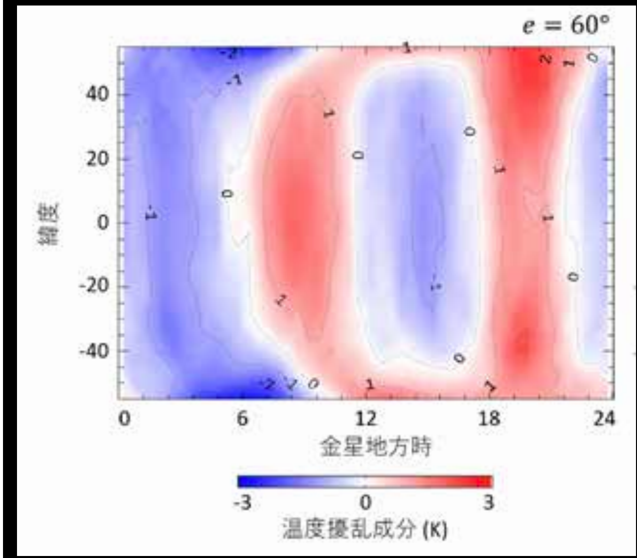

cloud-tracked winds

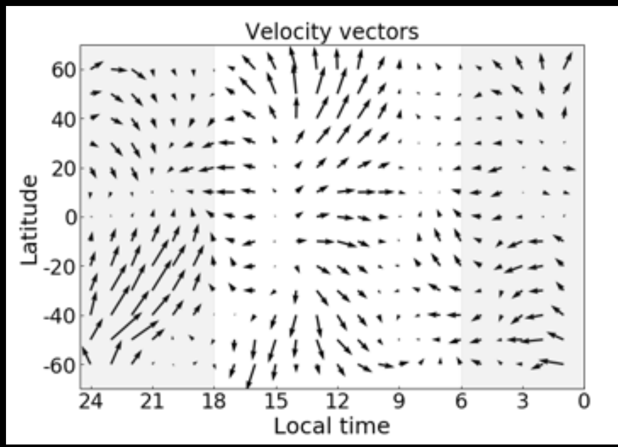

The waves will contribute to the maintenance of the fast atmospheric circulation

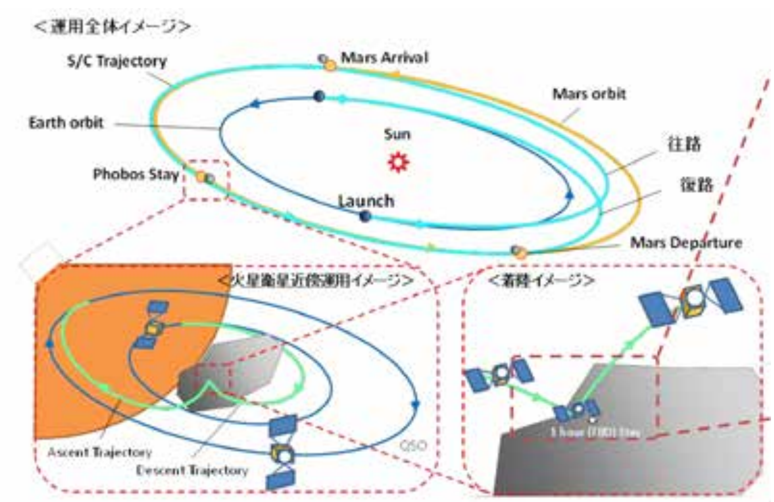

MMX: Martian Moons Exploration

- Mission to Mars/Phobos/Deimos
- Sample return from Phobos
- Three years in Mars orbit
- Target launch year is 2024

localized water vapor transport and phase change : keys to understand water cycle and reservoir stability

Thick clouds on nightside

Cloud belt

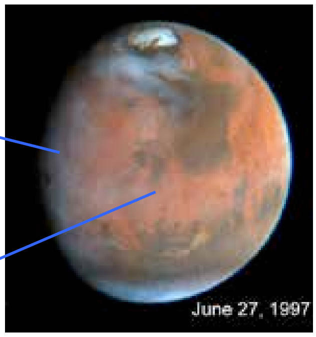

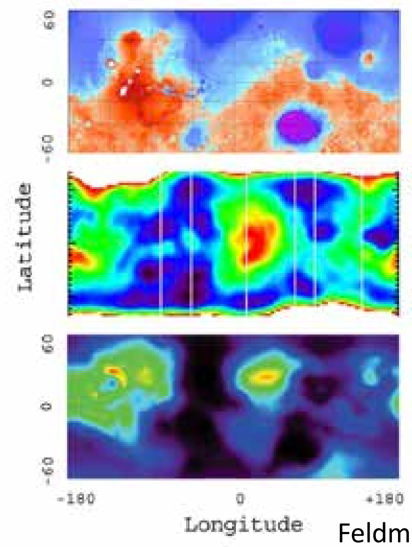

Water Equivalent Hydrogen

Precipitation predicted by GCM

Feldman et al. (2005)

Mars Express/PFS water vapor map

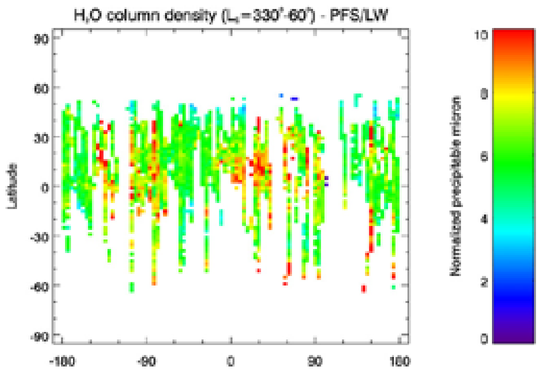

Fouchet et al. (2007)

Previous observations did not obtain snapshots of high-resolution water vapor distribution and did not observe formation/evaporation of localized clouds

Fast, localized dust storms : key to understand dust lifting and anomalous dust distribution

Meridional cross section of dust mixing ratio

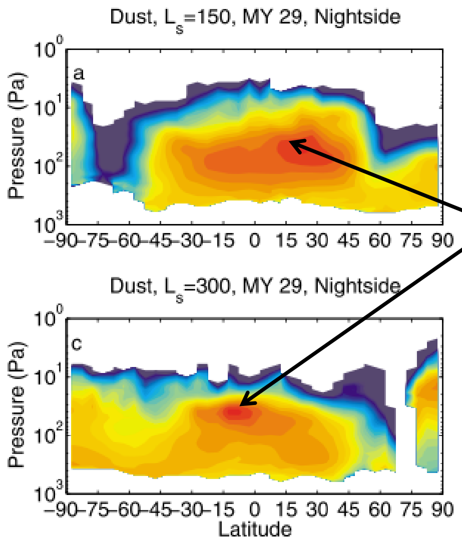

Detached dust layers

Heavens et al. (2011)

"Rocket dust storm": source of high-altitude dust ?

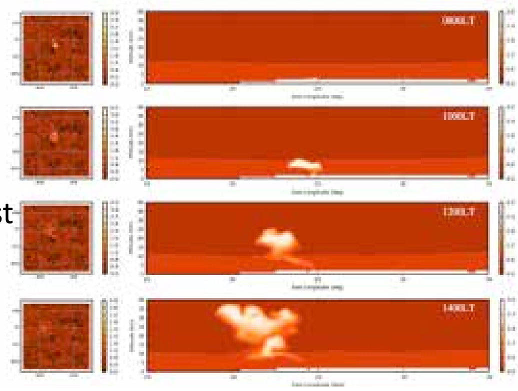

Spiga et al. (2013)

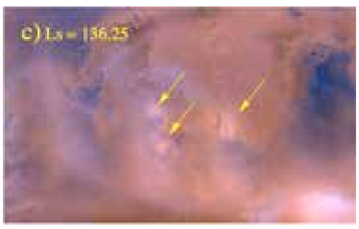

Localized dust clouds : Previous observations did not detect temporal development

High-altitude orbit of MMX: an ideal platform for continuous, high-resolution monitoring

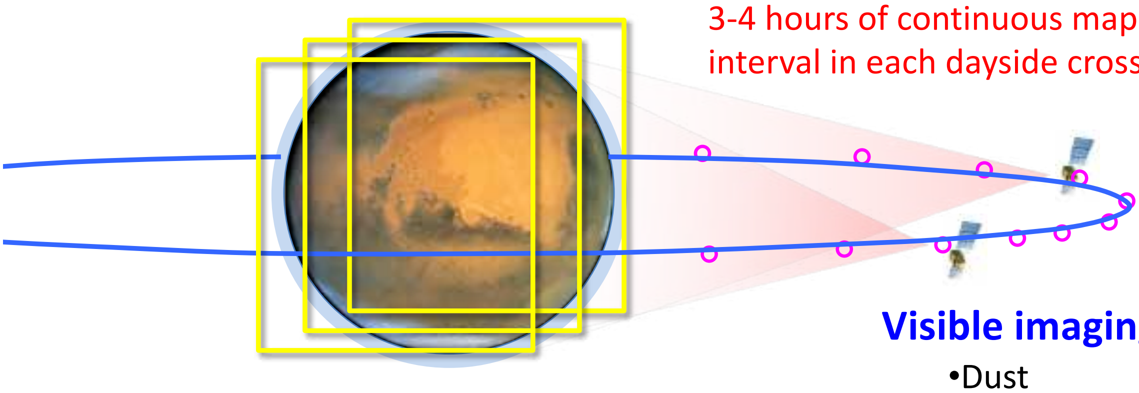

3-4 hours of continuous mapping at <1 h interval in each dayside crossing

Visible imaging
- Dust
- Cloud

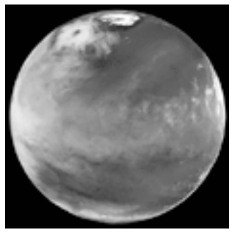

Near-IR Imaging spectroscopy
- Water vapor
- Dust, cloud
- Surface pressure
- CO

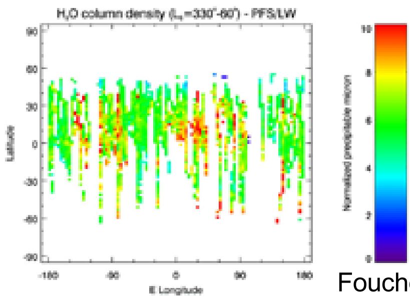

Fouchet et al. (2007)

Limitation of observations from polar, low-altitude orbiters

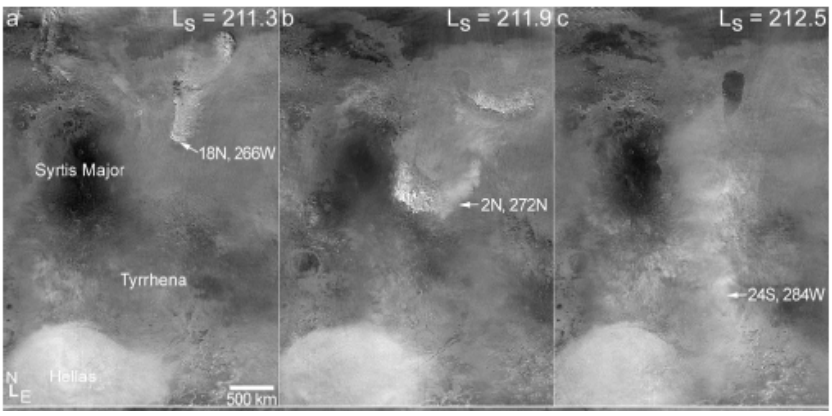

MOC images taken on three successive days
Too sparse in time

Concept of trace gas observations by Trace Gas Orbiter
Too sparse in space

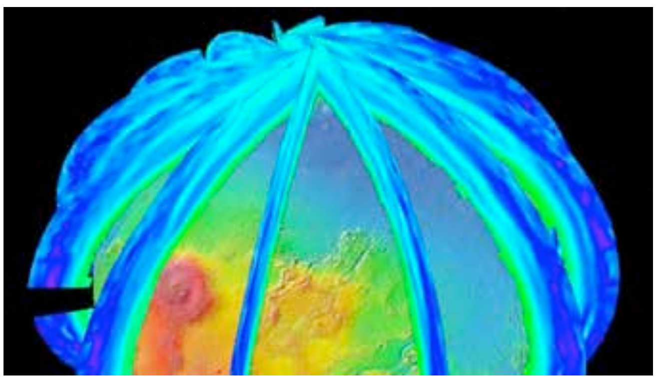

Phobos orbit